

IMPERIAL

**Reconfigurable Intelligent Surfaces:
Beamforming, Modulation, and Channel Shaping**

Yang Zhao

Supervisor: Prof. Bruno Clerckx

Department of Electrical and Electronic Engineering
Imperial College London

This dissertation is submitted for the degree of
Doctor of Philosophy

Declaration

I hereby declare that the contents presented in this dissertation are original and have been carried out by myself under the guidance of my supervisor Prof. Bruno Clerckx. Any work from other researchers, scholars, or sources have been properly cited and acknowledged. The contents have not been submitted in whole or in part for consideration of any other degree or qualification in any academic institution. I am aware of the ethical standards and academic integrity policies of Imperial College London, and I have adhered to these principles throughout the course of my study. In signing this declaration, I affirm my commitment to academic honesty, intellectual integrity, and the pursuit of knowledge in the service of truth and understanding.

The copyright of this thesis rests with the author. Unless otherwise indicated, its contents are licensed under a Creative Commons Attribution-Non Commercial 4.0 International License (CC BY-NC). Under this license, you may copy and redistribute the material in any medium or format. You may also create and distribute modified versions of the work. This is on the condition that: you credit the author and do not use it, or any derivative works, for a commercial purpose. When reusing or sharing this work, ensure you make the license terms clear to others by naming the license and linking to the license text. Where a work has been adapted, you should indicate that the work has been changed and describe those changes. Please seek permission from the copyright holder for uses of this work that are not included in this license or permitted under UK Copyright Law.

The source code of all simulation results in this dissertation are publicly available at <https://github.com/snowztail/>.

Yang Zhao
March 2024

Abstract

This is where you write your abstract ...

Table of contents

List of figures	ix
List of tables	xi
Abbreviations	xiii
Notation	xvii
1 Getting started	1
1.1 Introduction	1
1.1.1 Simultaneous Wireless Information and Power Transfer	1
1.1.2 Reconfigurable Intelligent Surface	2
1.1.3 RIS-Aided SWIPT	3
1.2 System Model	5
1.2.1 Transmitted Signal	5
1.2.2 Reflection Pattern and Composite Channel	6
1.2.3 Received Signal	7
1.2.4 Receiving Modes	7
1.2.5 Information Decoder	8
1.2.6 Energy Harvester	9
1.2.7 Rate-Energy Region	10
1.3 Problem Formulation	11
1.3.1 Passive Beamforming	12
1.3.2 Active Beamforming	14
1.3.3 Waveform and Splitting Ratio	15
1.3.4 Low-Complexity Adaptive Design	17
1.3.5 Block Coordinate Descent	19
1.4 Performance Evaluations	20
1.5 Conclusion and Future Works	28

References**31**

List of figures

1.1	An Reconfigurable Intelligent Surface (RIS)-aided multi-carrier Multiple-Input Single-Output (MISO) Simultaneous Wireless Information and Power Transfer (SWIPT) system.	5
1.2	Diagrams of practical co-located receivers.	8
1.3	Equivalent circuits of receive antenna and energy harvester.	9
1.4	$\mathbf{W}_{I/P}$ consists of $N \times N$ blocks of size $M \times M$. $\mathbf{W}_{I/P,k}$ keeps the k -th block diagonal of $\mathbf{W}_{I/P}$ and nulls all remaining blocks. Solid, dashed and dotted blocks correspond to $k > 0$, $k = 0$ and $k < 0$, respectively. For $\mathbf{w}_{I/P,n_1} \mathbf{w}_{I/P,n_2}^H$, the k -th block diagonal satisfies $k = n_2 - n_1$	10
1.5	System layout in simulation.	20
1.6	Sorted equivalent subchannel amplitude with and without RIS versus N for $M = 1$, $L = 100$, $\sigma_n^2 = -40$ dBm, $B = 10$ MHz and $d_H = d_V = 2$ m.	22
1.7	Average Rate-Energy (R-E) region and Wireless Power Transfer (WPT) waveform amplitude versus N for $M = 1$, $L = 20$, $\sigma_n^2 = -40$ dBm, $B = 1$ MHz and $d_H = d_V = 2$ m.	23
1.8	Average R-E region and splitting ratio versus σ_n^2 for $M = 1$, $N = 16$, $L = 20$, $B = 1$ MHz and $d_H = d_V = 2$ m.	23
1.9	Average R-E region and path loss versus d_H for $M = 1$, $N = 16$, $L = 20$, $\sigma_n^2 = -40$ dBm, $B = 1$ MHz and $d_V = 2$ m.	24
1.10	Average R-E region, Wireless Information Transfer (WIT) Signal-to-Noise Ratio (SNR) and WPT Direct Current (DC) versus M for $N = 16$, $L = 20$, $\sigma_n^2 = -40$ dBm, $B = 1$ MHz, $d_H = d_V = 0.2$ m.	25
1.11	Average R-E region, WIT SNR and WPT DC versus L for $M = 1$, $N = 16$, $\sigma_n^2 = -40$ dBm, $B = 1$ MHz and $d_H = d_V = 0.2$ m.	25
1.12	Average R-E region for ideal, adaptive, fixed and no RIS versus B for $M = 1$, $N = 16$, $L = 20$, $\sigma_n^2 = -40$ dBm and $d_H = d_V = 2$ m.	27

- 1.13 Average R-E region with imperfect cascaded Channel State Information at the Transmitter (CSI) and quantized RIS for $M = 1$, $N = 16$, $L = 20$, $\sigma_n^2 = -40$ dBm, $B = 10$ MHz and $d_H = d_V = 2$ m. $\epsilon_n = 0$ and $\epsilon_n = \infty$ correspond respectively to perfect CSIT and no CSIT (and random RIS); $b = 0$ and $b \rightarrow \infty$ correspond respectively to no RIS and continuous RIS. . 28

List of tables

Abbreviations

bpcu	bits per channel use
bps/Hz	bits per second per Hertz
AF	Amplify-and-Forward
AM	Arithmetic Mean
AmBC	Ambient Backscatter Communication
AO	Alternating Optimization
AP	Access Point
AWGN	Additive White Gaussian Noise
BackCom	Backscatter Communication
BBC	Bistatic Backscatter Communication
BCD	Block Coordinate Descent
BD	Beyond-Diagonal
BER	Bit Error Rate
BIBO	Binary-Input Binary-Output
BLS	Backtracking Line Search
CLT	Central Limit Theorem
CP	Canonical Polyadic
CR	Cognitive Radio
CSCG	Circularly Symmetric Complex Gaussian
CSI	Channel State Information
CSIT	Channel State Information at the Transmitter
CW	Continuous Waveform
DC	Direct Current
DCMC	Discrete-input Continuous-output Memoryless Channel

DF	Decode-and-Forward
DMC	Discrete Memoryless Channel
DMMAC	Discrete Memoryless Multiple Access Channel
DMTC	Discrete Memoryless Thresholding Channel
DoF	Degree of Freedom
DP	Dynamic Programming
EIRP	Effective Isotropic Radiated Power
FDMA	Frequency-Division Multiple Access
FPGA	Field-Programmable Gate Array
GM	Geometric Mean
GP	Geometric Programming
i.i.d.	independent and identically distributed
IC	Interference Channel
IoE	Internet of Everything
IoT	Internet of Things
KKT	Karush-Kuhn-Tucker
LC	Low-Complexity
LoS	Line-of-Sight
M2M	Machine-to-Machine
MAC	Multiple Access Channel
MBC	Monostatic Backscatter Communication
MC	Multiplication Coding
MIMO	Multiple-Input Multiple-Output
MISO	Multiple-Input Single-Output
ML	Maximum-Likelihood
MMSE	Minimum Mean-Square-Error
MRC	Maximal Ratio Combining
MRT	Maximum Ratio Transmission
MSE	Mean-Square Error

NLoS	Non-Line-of-Sight
NOMA	Non-Orthogonal Multiple Access
OFDM	Orthogonal Frequency-Division Multiplexing
PC	Point-to-point Channel
PDF	Probability Density Function
PGA	Projected Gradient Ascent
PIN	Positive Intrinsic Negative
PS	Power Splitting
PSK	Phase Shift Keying
QAM	Quadrature Amplitude Modulation
QoS	Quality of Service
R-E	Rate-Energy
RCG	Riemannian Conjugate Gradient
RF	Radio-Frequency
RFID	Radio-Frequency Identification
RIS	Reconfigurable Intelligent Surface
SC	Superposition Coding
SCA	Successive Convex Approximation
SDMA	Space-Division Multiple Access
SDP	Semi-Definite Programming
SDR	Semi-Definite Relaxation
SIC	Successive Interference Cancellation
SIMO	Single-Input Multiple-Output
SINR	Signal-to-Interference-plus-Noise Ratio
SISO	Single-Input Single-Output
SMAWK	Shor-Moran-Aggarwal-Wilber-Klawe
SMF	Scaled Matched Filter
SNR	Signal-to-Noise Ratio
SR	Symbiotic Radio
SVD	Singular Value Decomposition

SWIPT	Simultaneous Wireless Information and Power Transfer
TDMA	Time-Division Multiple Access
TS	Time Switching
UE	User Equipment
WF	Water-Filling
WIT	Wireless Information Transfer
WPCN	Wireless Powered Communication Network
WPT	Wireless Power Transfer
ZF	Zero-Forcing

Notation

Constants

e	Euler's number $\simeq 2.71828 \dots$
j	The imaginary unit $= \sqrt{-1}$
π	Archimedes' constant $\simeq 3.14159 \dots$

Objects

a, A	Scalar
\mathbf{a}	Column vector
\mathbf{A}	Matrix
\mathcal{A}	Finite set
$\mathbf{0}$	Zero matrix
$\mathbf{1}$	One matrix
\mathbf{I}	Identity matrix

Sets

\mathbb{R}	Real numbers
\mathbb{R}_+	Real nonnegative numbers
\mathbb{C}	Complex numbers
\mathbb{I}	Probability domain $[0, 1]$
$\mathbb{H}_+^{n \times n}$	Positive semi-definite matrices of dimension $n \times n$
$\mathbb{U}^{n \times n}$	Unitary matrices of dimension $n \times n$

Operations

$(\cdot)^*$	Complex conjugate
$(\cdot)^T$	Transpose
$(\cdot)^H$	Hermitian (conjugate transpose)
$(\cdot)^\dagger$	Moore-Penrose inverse

$(\cdot)^+$	Ramp function $\max(0, \cdot)$
$ \cdot $	Absolute value of a complex number
$\ \cdot\ $	Euclidean norm of a vector
$\ \cdot\ _F$	Frobenius norm of a matrix
$\arg(\cdot)$	Argument of a complex number
$\text{card}(\cdot)$	Cardinality of a finite set
$\log(\cdot)$	Natural logarithm of a real number
$\exp(\cdot)$	Exponential of a scalar or square matrix
$\text{tr}(\cdot)$	Trace of a square matrix
$\det(\cdot)$	Determinant of a square matrix
$\text{sv}(\cdot)$	Singular values sorted from largest to smallest
$\text{diag}(\cdot)$	Constructs a square matrix with inputs on the main diagonal
$\text{diag}^{-1}(\cdot)$	Retrieves the main diagonal of a square matrix
$\Re(\cdot)$	Retrieves the real part of a complex number
$\Im(\cdot)$	Retrieves the imaginary part of a complex number
$\mathbb{E}(\cdot)$	Expectation operator
$\mathbb{A}(\cdot)$	Extracts the Direct Current component of a signal
\odot	Hadamard product
\otimes	Kronecker product
$(\cdot)_{[x:y]}$	Shortcut for $(\cdot)_x, (\cdot)_{x+1}, \dots, (\cdot)_y$

Distributions

\sim	Follows a distribution
$\mathcal{CN}(\mathbf{0}, \Sigma)$	Multivariate Circularly Symmetric Complex Gaussian with covariance Σ

Subscripts

$(\cdot)_B$	Backward
$(\cdot)_D$	Direct
$(\cdot)_F$	Forward
$(\cdot)_I$	Information
$(\cdot)_P$	Power

Superscripts

$(\cdot)^{(r)}$	r -th iterated value
$(\cdot)^*$	Stationary point

Chapter 1

Getting started

1.1 Introduction

1.1.1 Simultaneous Wireless Information and Power Transfer

With the great advance in communication performance, a bottleneck of wireless networks has come to energy supply. Simultaneous Wireless Information and Power Transfer (SWIPT) is a promising solution to connect and power mobile devices via Radio-Frequency (RF) waves. It provides low power at μW level but broad coverage up to hundreds of meters in a sustainable and controllable manner, bringing more opportunities to the Internet of Things (IoT) and Machine-to-Machine (M2M) networks. The upsurge in wireless devices, together with the decrease of electronics power consumption, calls for a re-thinking of future wireless networks based on Wireless Power Transfer (WPT) and SWIPT [1].

The concept of SWIPT was first cast in [2], where the authors investigated the Rate-Energy (R-E) tradeoff for a flat Gaussian channel and typical discrete channels. [3] proposed two practical co-located information and power receivers, i.e., Time Switching (TS) and Power Splitting (PS). Dedicated information and energy beamforming were then investigated in [4, 5] to characterize the R-E region for multi-antenna broadcast and interference channels. On the other hand, [6] pointed out that the RF-to-Direct Current (DC) conversion efficiency of rectifiers depends on the input power and waveform shape. It implies that the modeling of the energy harvester, particularly its nonlinearity, has a crucial impact on the waveform preference, resource allocation, and system design of any wireless-powered systems [6, 7, 1]. Motivated by this, [8] derived a tractable nonlinear harvester model based on the Taylor expansion of diode I-V characteristics, and performed joint waveform and beamforming design for WPT. Simulation and experiments showed the benefit of modeling energy harvester nonlinearity in real system design [9, 10] and demonstrated the joint waveform and beamforming strategy as a

key technique to expand the operation range [11]. A low-complexity adaptive waveform design by Scaled Matched Filter (SMF) was proposed in [12] to exploit the rectifier nonlinearity, whose advantage was then demonstrated in a prototype with channel acquisition [13]. Beyond WPT, [14] uniquely showed that the rectifier nonlinearity brings radical changes to SWIPT design, namely (i) modulated and unmodulated waveforms are not equally suitable for wireless power delivery; (ii) a multi-carrier unmodulated waveform superposed to a multi-carrier modulated waveform can enlarge the R-E region; (iii) a combination of PS and TS is generally the best strategy; (iv) the optimal input distribution is not the conventional Circularly Symmetric Complex Gaussian (CSCG); (v) modeling rectifier nonlinearity is beneficial to system performance and essential to efficient SWIPT design. Those observations, validated experimentally in [9], led to the question: *What is the optimal input distribution for SWIPT under nonlinearity?* This question was answered in [15] for single-carrier SWIPT, and some attempts were further made in [16] for multi-carrier SWIPT. The answers shed new light to the fundamental limits of SWIPT and practical signaling (e.g., modulation and waveform) strategies. It is now well understood from [14–16] that, due to harvester nonlinearity, a combination of CSCG and on-off keying in single-carrier setting and non-zero mean asymmetric inputs in multi-carrier setting lead to significantly larger R-E region compared to conventional CSCG. Recently, [17] used machine learning techniques to design SWIPT signaling under nonlinearity to complement the information-theoretic results of [15], and new modulation schemes were subsequently invented.

1.1.2 Reconfigurable Intelligent Surface

Reconfigurable Intelligent Surface (RIS) has recently emerged as a promising technique that adapts the propagation environment to enhance the spectrum and energy efficiency. In practice, a RIS consists of multiple individual sub-wavelength reflecting elements to adjust the amplitude and phase of the incoming signal (i.e., passive beamforming). Different from the relay, backscatter and frequency-selective surface [18], the RIS assists the primary transmission using passive components with negligible thermal noise but is limited to frequency-dependent reflection.

Inspired by the development of real-time reconfigurable metamaterials [19], the authors of [20] introduced a programmable metasurface that steers or polarizes the electromagnetic wave at a specific frequency to mitigate signal attenuation. [21] proposed a RIS-assisted Multiple-Input Single-Output (MISO) system and jointly optimized the precoder at the Access Point (AP) and the phase shifts at the RIS to minimize the transmit power. The active and passive beamforming problem was then extended to the discrete phase shift case [22] and the multi-user case [23]. In [24], the authors investigated the impact of non-zero resistance on the

reflection pattern and emphasized the coupling between reflection amplitude and phase shift in practice. To estimate the cascaded AP-RIS-User Equipment (UE) link without RF-chains at the RIS, practical protocols were developed based on element-wise on/off switching [25], training sequence and reflection pattern design [26, 27], and compressed sensing [28]. The hardware architecture, design challenges, and application opportunities of practical RIS were covered in [29]. In [30], a prototype RIS with 256 2-bit elements based on Positive Intrinsic Negative (PIN) diodes was developed to support real-time video transmission at GHz and mmWave frequency.

1.1.3 RIS-Aided SWIPT

By integrating RIS with SWIPT, the constructive reflection can boost the end-to-end power efficiency and improve the R-E tradeoff. In multi-user cases, dedicated energy beams were proved unnecessary for the weighted sum-power maximization [31] but essential when fairness issue is considered [32]. It was also claimed that Line-of-Sight (LoS) links could boost the power efficiency since rank-deficient channels require fewer energy beams [33]. However, [31–33] were based on a linear energy harvester model that is known in both the RF and the communication literature to be inefficient and inaccurate [1, 6–17]. Based on practical RIS and harvester models, [34] introduced a scalable resource allocation framework for a large-scale tile-based RIS-assisted SWIPT system, where the optimization consists of a reflection design stage and a joint reflection selection and precoder design stage. The proposed framework provides a flexible tradeoff between performance and complexity. To the best of our knowledge, all existing papers considered resource allocation and beamforming design for dedicated information and energy users in a single-carrier network. In this paper, we instead build our design based on a proper nonlinear harvester model that captures the dependency of the output DC power on both the power and shape of the input waveform, and marry the benefits of joint multi-carrier waveform and active beamforming optimization for SWIPT with the passive beamforming capability of RIS, to investigate the R-E tradeoff for one SWIPT user with co-located information decoder and energy harvester. We ask ourselves the important question: *How to jointly exploit the spatial domain and the frequency domain efficiently through joint waveform and beamforming design to enlarge the R-E region of RIS-aided SWIPT?* The contributions of this paper are summarized as follows.

First, we propose a novel RIS-aided SWIPT architecture based on joint waveform, active and passive beamforming design under the diode nonlinear model [8]. Although this tractable harvester model accurately reveals how the input power level and waveform shape influence the output DC power, it also introduces design challenges such as frequency coupling (i.e., components of different frequencies compensate and produce DC), waveform coupling (i.e.,

different waveforms jointly contribute to DC), and high-order objective function. To make an efficient use of the rectifier nonlinearity, we superpose a multi-carrier unmodulated power waveform (deterministic multisine) to a multi-carrier modulated information waveform and evaluate the performance under the TS and PS receiving modes. The proposed joint waveform, active and passive beamforming architecture exploits the rectifier nonlinearity, the channel selectivity, and a beamforming gain across frequency and spatial domains to enlarge the achievable R-E region. This is the first paper to propose a joint waveform, active and passive beamforming architecture for RIS-aided SWIPT.

Second, we characterize each R-E boundary point by energy maximization under a rate constraint. The problem is solved by a Block Coordinate Descent (BCD) algorithm based on the Channel State Information at the Transmitter (CSI). For active beamforming, we prove that the global optimal active information and power precoders coincide at Maximum Ratio Transmission (MRT) even with rectifier nonlinearity. For passive beamforming, we propose a Successive Convex Approximation (SCA) algorithm and retrieve the RIS phase shift by eigen decomposition with optimality proof. Finally, the superposed waveform and the splitting ratio are optimized by the Geometric Programming (GP) technique. The RIS phase shift, active precoder, and waveform amplitude are updated iteratively until convergence. This is the first paper to jointly optimize waveform and active/passive beamforming in RIS-aided SWIPT.

Third, we introduce two closed-form adaptive waveform schemes to avoid the exponential complexity of the GP algorithm. To facilitate practical SWIPT implementation, the Water-Filling (WF) strategy for modulated waveform and the SMF strategy for multisine waveform are combined in time and power domains, respectively. The passive beamforming design is also adapted to accommodate the low-complexity waveform schemes. The proposed low-complexity BCD algorithm achieves a good balance between performance and complexity.

Fourth, we provide numerical results to evaluate the proposed algorithms. It is concluded that (i) RIS enables constructive reflection and flexible subchannel design in the frequency domain that is essential for SWIPT systems; (ii) RIS mainly affects the effective channel instead of the waveform design; (iii) multisine waveform is beneficial to energy transfer especially when the number of subbands is large; (iv) TS is preferred at low Signal-to-Noise Ratio (SNR) while PS is preferred at high SNR; (v) there exist two optimal RIS development locations, one close to the AP and one close to the UE; (vi) the output SNR scales linearly with the number of transmit antennas and quadratically with the number of RIS elements; (vii) due to the rectifier nonlinearity, the output DC scales quadratically with the number of transmit antennas and quartically with the number of RIS elements; (viii) for narrowband SWIPT, the optimal active and passive beamforming for any R-E point are also optimal for the whole R-E region; (ix) for broadband SWIPT, the optimal active and passive beamforming

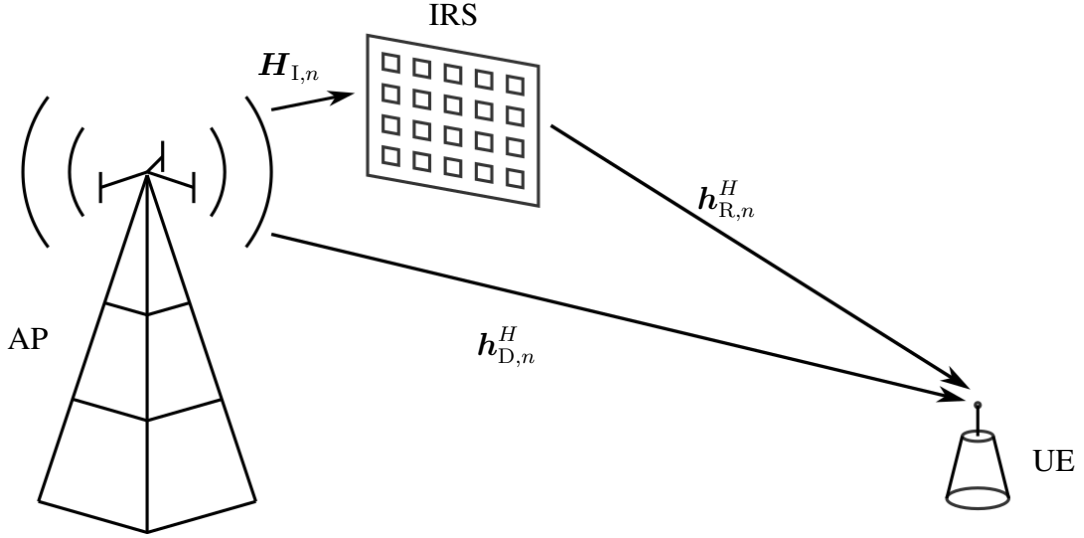


Fig. 1.1 An RIS-aided multi-carrier MISO SWIPT system.

depend on specific R-E point and require adaptive designs; (x) the proposed algorithms are robust to practical impairments such as inaccurate cascaded CSIT and finite RIS reflection states.

1.2 System Model

As shown in Fig. 1.1, we propose a RIS-aided SWIPT system where an M -antenna AP delivers information and power simultaneously, through an L -element RIS, to a single-antenna UE over N orthogonal evenly-spaced subbands. We consider a quasi-static block fading model and assume the CSIT of direct and cascaded channels is known. The signals reflected by two or more times are omitted, and the noise power is assumed too small to be harvested.

1.2.1 Transmitted Signal

Following [14], we superpose a multi-carrier modulated information-bearing waveform to a multi-carrier unmodulated power-dedicated deterministic multisine to boost the spectrum and energy efficiency. The information signal transmitted over subband $n \in \{1, \dots, N\}$ at time t is

$$\mathbf{x}_{I,n}(t) = \Re \{ \mathbf{w}_{I,n} \tilde{x}_{I,n}(t) e^{j2\pi f_n t} \}, \quad (1.1)$$

where $\mathbf{w}_{I,n} \in \mathbb{C}^{M \times 1}$ is the information precoder at subband n , $\tilde{x}_{I,n} \sim \mathcal{CN}(0, 1)$ is the information symbol at subband n , and f_n is the frequency of subband n . On the other hand,

the power signal transmitted over subband n at time t is

$$\mathbf{x}_{P,n}(t) = \Re \left\{ \mathbf{w}_{P,n} e^{j2\pi f_n t} \right\}, \quad (1.2)$$

where $\mathbf{w}_{P,n} \in \mathbb{C}^{M \times 1}$ is the power precoder at subband n . Therefore, the superposed signal transmitted over all subbands at time t is

$$\mathbf{x}(t) = \Re \left\{ \sum_{n=1}^N (\mathbf{w}_{I,n} \tilde{x}_{I,n}(t) + \mathbf{w}_{P,n}) e^{j2\pi f_n t} \right\}. \quad (1.3)$$

We also define $\mathbf{w}_{I/P} \triangleq [\mathbf{w}_{I/P,1}^T, \dots, \mathbf{w}_{I/P,N}^T]^T \in \mathbb{C}^{MN \times 1}$.

1.2.2 Reflection Pattern and Composite Channel

According to Green's decomposition [35], the backscattered signal of an antenna can be decomposed into the *structural mode* component and the *antenna mode* component. The former is fixed and can be regarded as part of the environment multipath, while the latter is adjustable and depends on the mismatch of the antenna and load impedance. RIS element $l \in \{1, \dots, L\}$ varies its impedance $Z_l = R_l + jX_l$ to reflect the incoming signal, and the reflection coefficient is defined as

$$\phi_l = \frac{Z_l - Z_0}{Z_l + Z_0} \triangleq \eta_l e^{j\theta_l}, \quad (1.4)$$

where Z_0 is the real-valued characteristic impedance, $\eta_l \in [0, 1]$ is the reflection amplitude,¹ and $\theta_l \in [0, 2\pi)$ is the phase shift. We also define $\boldsymbol{\phi} \triangleq [\phi_1, \dots, \phi_L]^H \in \mathbb{C}^{L \times 1}$ and $\boldsymbol{\Theta} \triangleq \text{diag}(\phi_1, \dots, \phi_L) = \text{diag}(\boldsymbol{\Phi}^*) \in \mathbb{C}^{L \times L}$ as the RIS vector and matrix, respectively.

Remark 1. *The element impedance Z_l maps to the reflection coefficient ϕ_l uniquely. Since the reactance X_l depends on the frequency, the reflection coefficient ϕ_l is also a function of frequency and cannot be designed independently at different subbands. In this paper, we assume the bandwidth is small compared to the operating frequency such that the reflection coefficient of each RIS element is the same at all subbands.*

At subband n , we denote the AP-UE direct channel as $\mathbf{h}_{D,n}^H \in \mathbb{C}^{1 \times M}$, the AP-RIS incident channel as $\mathbf{H}_{I,n} \in \mathbb{C}^{L \times M}$, and the RIS-UE reflected channel as $\mathbf{h}_{R,n}^H \in \mathbb{C}^{1 \times L}$. The auxiliary AP-RIS-UE link can be modeled as a concatenation of the incident channel, the RIS reflection,

¹Due to the non-zero power consumption at the RIS, $R_l > 0$ in practice such that $\eta_l < 1$ and is a function of θ_l . This paper sticks to the most common RIS model where the reflection amplitude equals 1 so as to reduce the design complexity and provide a primary benchmark for practical RIS-aided SWIPT.

and the reflected channel. Hence, the composite equivalent channel reduces to

$$\mathbf{h}_n^H = \mathbf{h}_{D,n}^H + \mathbf{h}_{R,n}^H \Theta \mathbf{H}_{I,n} = \mathbf{h}_{D,n}^H + \phi^H \mathbf{V}_n, \quad (1.5)$$

where we define the cascaded incident-reflected channel at subband n as $\mathbf{V}_n \triangleq \text{diag}(\mathbf{h}_{R,n}^H) \mathbf{H}_{I,n} \in \mathbb{C}^{L \times M}$. We also define $\mathbf{h} \triangleq [\mathbf{h}_1^T, \dots, \mathbf{h}_N^T]^T \in \mathbb{C}^{MN \times 1}$.

Remark 2. *The cascaded channel varies at different subbands, but the reflection cannot be designed independently at different frequencies. Therefore, there exists a tradeoff for the passive beamforming design in the frequency domain, and the composite subchannels should be tuned adaptively to meet the specific requirement of multi-carrier SWIPT. For example, one can design the reflection pattern to either enhance the strongest subband (e.g., $\max_{\phi, n} \|\mathbf{h}_n\|$), or improve the fairness among subbands (e.g., $\max_{\phi} \min_n \|\mathbf{h}_n\|$). That is to say, RIS essentially enables a flexible subchannel design. In the MISO case, a similar effect also exists in the spatial domain. Therefore, each reflection coefficient is indeed shared by M antennas over N subbands.*

1.2.3 Received Signal

The received superposed signal at the single-antenna UE is²

$$y(t) = \Re \left\{ \sum_{n=1}^N \left(\mathbf{h}_n^H (\mathbf{w}_{I,n} \tilde{x}_{I,n}(t) + \mathbf{w}_{P,n}) + \tilde{n}_n(t) \right) e^{j2\pi f_n t} \right\}, \quad (1.6)$$

where $\tilde{n}_n(t)$ is the noise at RF band n . Note that the modulated component can be used for energy harvesting if necessary, but the multisine component carries no information and cannot be used for information decoding.

1.2.4 Receiving Modes

As illustrated in Fig. 1.2, there are two practical receiving modes for the co-located information decoder and energy harvester [3]. The TS receiver divides each transmission block into orthogonal data and energy sessions with duration $1 - \eta$ and η , respectively. During each session, the transmitter optimizes the waveform for either Wireless Information Transfer (WIT) or WPT, while the receiver activates the information decoder or the energy harvester correspondingly. The duration ratio η controls the R-E tradeoff and is independent from the

²We assume that the time difference of signal arrival via direct and auxiliary link is negligible compared to the symbol period.

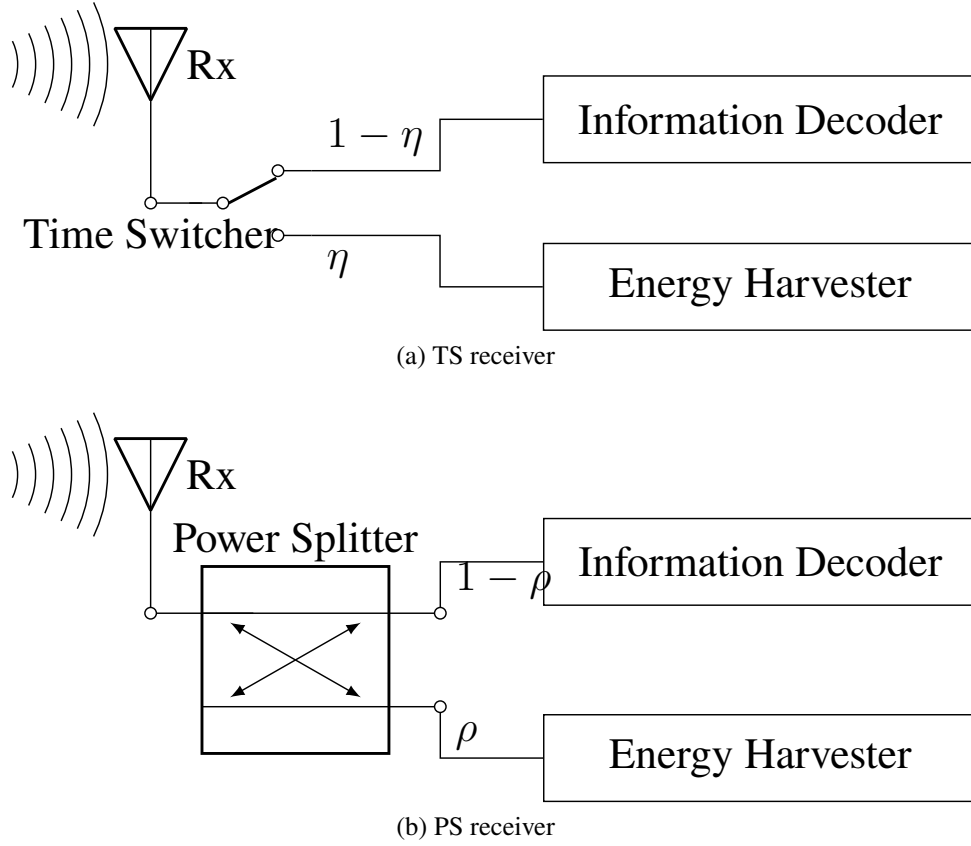


Fig. 1.2 Diagrams of practical co-located receivers.

waveform and beamforming design. On the other hand, the PS receiver splits the incoming signal into individual data and energy streams with power ratio $1 - \rho$ and ρ , respectively. The data stream is fed into the information decoder while the energy stream is fed into the energy harvester. During each transmission block, the superposed waveform and splitting ratio are jointly designed to achieve different R-E tradeoffs. In the following context, we consider the optimization with the PS receiver, as the TS receiver can be regarded as a special case (i.e., a time sharing between $\rho = 0$ and $\rho = 1$).

1.2.5 Information Decoder

A major benefit of the superposed waveform is that the multisine is deterministic and creates no interference to the modulated waveform [14]. Therefore, the achievable rate is³

$$R(\phi, \mathbf{w}_I, \rho) = \sum_{n=1}^N \log_2 \left(1 + \frac{(1 - \rho) |\mathbf{h}_n^H \mathbf{w}_{I,n}|^2}{\sigma_n^2} \right), \quad (1.7)$$

³It requires waveform cancellation or translated demodulation [14].

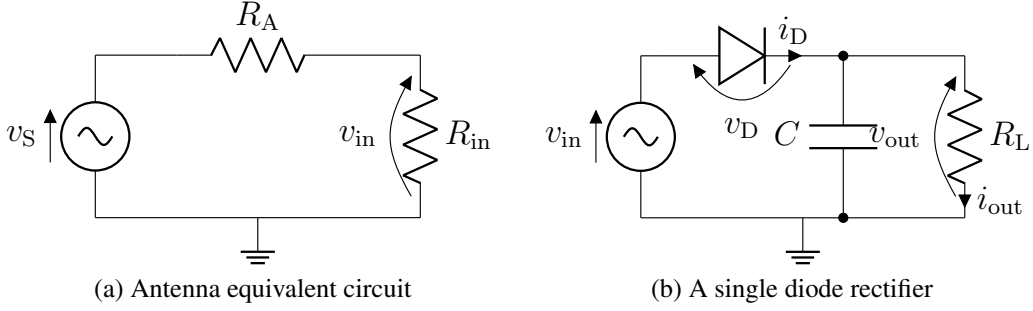


Fig. 1.3 Equivalent circuits of receive antenna and energy harvester.

where σ_n^2 is the noise variance at the RF-band and during the RF-to-baseband conversion on tone n .

1.2.6 Energy Harvester

Taken from [8], the rectenna model used in this section captures the dependency of the output DC on both the power and shape of the received signal. Fig. 1.3(a) illustrates the equivalent circuit of an ideal antenna, where the antenna has a resistance R_A and the incoming signal creates a voltage source $v_S(t)$. Let R_{in} be the total input resistance of the rectifier and matching network, and we assume the voltage across the matching network is negligible. When perfectly matched (i.e., $R_{in} = R_A$), the rectifier input voltage is $v_{in}(t) = y(t)\sqrt{\rho R_A}$. Consider a simplified rectifier model in Fig. 1.3(b) where a single series diode is followed by a low-pass filter with a parallel load. As detailed in [14], a truncated Taylor expansion of the diode I-V characteristic equation suggests that maximizing the average output DC is equivalent to maximizing a monotonic function⁴

$$z(\phi, \mathbf{w}_I, \mathbf{w}_P, \rho) = \sum_{i \text{ even}, i \geq 2}^{n_0} k_i \rho^{i/2} R_A^{i/2} \mathbb{E} \{ \mathbb{A} \{ y(t)^i \} \}, \quad (1.8)$$

where n_0 is the truncation order and $k_i \triangleq i_S / i! (n' v_T)^i$ is the diode coefficient (i_S is the reverse bias saturation current, n' is the diode ideality factor, v_T is the thermal voltage). With a slight abuse of notation, we refer to z as the average output DC in this paper. It can be observed that the conventional linear harvester model, where the output DC power equals the sum of the power harvested on each frequency, is a special case of (1.8) with $n_0 = 2$. However, due to the coupling effect among different frequencies, some high-order frequency components

⁴This small-signal expansion model is only valid for the nonlinear operation region of the diode, and the I-V relationship would be linear if the diode behavior is dominated by the load [8].

$$\mathbf{W}_{I/P} = \begin{pmatrix} \boxed{\mathbf{w}_{I/P,1}\mathbf{w}_{I/P,1}^H} & \boxed{\mathbf{w}_{I/P,1}\mathbf{w}_{I/P,2}^H} & \cdots & \boxed{\mathbf{w}_{I/P,1}\mathbf{w}_{I/P,N}^H} \\ \boxed{\mathbf{w}_{I/P,2}\mathbf{w}_{I/P,1}^H} & \boxed{\mathbf{w}_{I/P,2}\mathbf{w}_{I/P,2}^H} & \ddots & \vdots \\ \vdots & \ddots & \ddots & \mathbf{w}_{I/P,N-1}\mathbf{w}_{I/P,N}^H \\ \boxed{\mathbf{w}_{I/P,N}\mathbf{w}_{I/P,1}^H} & \cdots & \mathbf{w}_{I/P,N}\mathbf{w}_{I/P,N-1}^H & \boxed{\mathbf{w}_{I/P,N}\mathbf{w}_{I/P,N}^H} \end{pmatrix} \begin{matrix} \leftarrow k=1 \\ \leftarrow k=0 \\ \leftarrow k=-1 \end{matrix}$$

Fig. 1.4 $\mathbf{W}_{I/P}$ consists of $N \times N$ blocks of size $M \times M$. $\mathbf{W}_{I/P,k}$ keeps the k -th block diagonal of $\mathbf{W}_{I/P}$ and nulls all remaining blocks. Solid, dashed and dotted blocks correspond to $k > 0$, $k = 0$ and $k < 0$, respectively. For $\mathbf{w}_{I/P,n_1}\mathbf{w}_{I/P,n_2}^H$, the k -th block diagonal satisfies $k = n_2 - n_1$.

compensate each other in frequency and further contribute to the output DC power. In other words, even-order terms with $i \geq 4$ account for the nonlinear diode behavior. For simplicity, we choose $n_0 = 4$ to investigate the fundamental rectifier nonlinearity, and define $\beta_2 \triangleq k_2 R_A$, $\beta_4 \triangleq k_4 R_A^2$ to rewrite z by (1.9). Note that $\mathbb{E}\{|\tilde{x}_{I,n}|^2\} = 1$ but $\mathbb{E}\{|\tilde{x}_{I,n}|^4\} = 2$ applies a modulation gain on the fourth-order DC terms. Let $\mathbf{W}_{I/P} \triangleq \mathbf{w}_{I/P}\mathbf{w}_{I/P}^H \in \mathbb{C}^{MN \times MN}$. As illustrated by Fig. 1.4, $\mathbf{W}_{I/P}$ can be divided into $N \times N$ blocks of size $M \times M$, and we let $\mathbf{W}_{I/P,k}$ keep its block diagonal $k \in \{-N+1, \dots, N-1\}$ and set all other blocks to 0. Hence, the components of z reduce to (1.10)–(1.13) [36].

1.2.7 Rate-Energy Region

The achievable R-E region is defined as

$$\mathcal{C}_{R-E} \triangleq \left\{ (R_{ID}, z_{EH}) \in \mathbb{R}_+^2 \mid R_{ID} \leq R, z_{EH} \leq z, \right. \\ \left. \frac{1}{2} (\|\mathbf{w}_I\|^2 + \|\mathbf{w}_P\|^2) \leq P \right\}, \quad (1.14)$$

where P is the average transmit power budget and $1/2$ converts the peak value of the sine waves to the average value.

1.3 Problem Formulation

We characterize each R-E boundary point through a current maximization problem subject to sum rate, transmit power, and reflection amplitude constraints as

$$\max_{\phi, \mathbf{w}_I, \mathbf{w}_P, \rho} z(\phi, \mathbf{w}_I, \mathbf{w}_P, \rho) \quad (1.15a)$$

$$\text{s.t.} \quad R(\phi, \mathbf{w}_I, \rho) \geq \bar{R}, \quad (1.15b)$$

$$\frac{1}{2} (\|\mathbf{w}_I\|^2 + \|\mathbf{w}_P\|^2) \leq P, \quad (1.15c)$$

$$|\phi| = 1, \quad (1.15d)$$

$$0 \leq \rho \leq 1. \quad (1.15e)$$

Problem (1.15) is intricate because of the coupled variables in (1.15a), (1.15b) and the non-convex constraint (1.15d). To obtain a feasible solution, we propose a BCD algorithm that iteratively updates (i) the RIS phase shift; (ii) the active precoder; (iii) the waveform amplitude and splitting ratio, until convergence.

$$z(\phi, \mathbf{w}_I, \mathbf{w}_P, \rho) = \beta_2 \rho \left(\mathbb{E} \{ \mathbb{A} \{ y_I^2(t) \} \} + \mathbb{A} \{ y_P^2(t) \} \right) + \beta_4 \rho^2 \left(\mathbb{E} \{ \mathbb{A} \{ y_I^4(t) \} \} + \mathbb{A} \{ y_P^4(t) \} + 6 \mathbb{E} \{ \mathbb{A} \{ y_I^2(t) \} \mathbb{A} \{ y_P^2(t) \} \} \right) \quad (1.9)$$

$$\mathbb{E} \{ \mathbb{A} \{ y_I^2(t) \} \} = \frac{1}{2} \sum_{n=1}^N (\mathbf{h}_n^H \mathbf{w}_{I,n}) (\mathbf{h}_n^H \mathbf{w}_{I,n})^* = \frac{1}{2} \mathbf{h}^H \mathbf{W}_{I,0} \mathbf{h}, \quad (1.10)$$

$$\mathbb{E} \{ \mathbb{A} \{ y_I^4(t) \} \} = \frac{3}{4} \left(\sum_{n=1}^N (\mathbf{h}_n^H \mathbf{w}_{I,n}) (\mathbf{h}_n^H \mathbf{w}_{I,n})^* \right)^2 = \frac{3}{4} (\mathbf{h}^H \mathbf{W}_{I,0} \mathbf{h})^2, \quad (1.11)$$

$$\mathbb{A} \{ y_P^2(t) \} = \frac{1}{2} \sum_{n=1}^N (\mathbf{h}_n^H \mathbf{w}_{P,n}) (\mathbf{h}_n^H \mathbf{w}_{P,n})^* = \frac{1}{2} \mathbf{h}^H \mathbf{W}_{P,0} \mathbf{h}, \quad (1.12)$$

$$\mathbb{A} \{ y_P^4(t) \} = \frac{3}{8} \sum_{\substack{n_1, n_2, n_3, n_4 \\ n_1 + n_2 = n_3 + n_4}} (\mathbf{h}_{n_1}^H \mathbf{w}_{P,n_1}) (\mathbf{h}_{n_2}^H \mathbf{w}_{P,n_2}) (\mathbf{h}_{n_3}^H \mathbf{w}_{P,n_3})^* (\mathbf{h}_{n_4}^H \mathbf{w}_{P,n_4})^* = \frac{3}{8} \sum_{k=-N+1}^{N-1} (\mathbf{h}^H \mathbf{W}_{P,k} \mathbf{h}) (\mathbf{h}^H \mathbf{W}_{P,-k} \mathbf{h}) \quad (1.13)$$

1.3.1 Passive Beamforming

In this section, we optimize the RIS phase shift ϕ for any given waveform $\mathbf{w}_{I/P}$ and splitting ratio ρ . Note that

$$\begin{aligned}
 |\mathbf{h}_n^H \mathbf{w}_{I,n}|^2 &= \mathbf{w}_{I,n}^H \mathbf{h}_n \mathbf{h}_n^H \mathbf{w}_{I,n} \\
 &= \mathbf{w}_{I,n}^H (\mathbf{h}_{D,n} + \mathbf{V}_n^H \phi) (\mathbf{h}_{D,n}^H + \phi^H \mathbf{V}_n) \mathbf{w}_{I,n} \\
 &= \mathbf{w}_{I,n}^H \mathbf{M}_n^H \Phi \mathbf{M}_n \mathbf{w}_{I,n} \\
 &= \text{tr}(\mathbf{M}_n \mathbf{w}_{I,n} \mathbf{w}_{I,n}^H \mathbf{M}_n^H \Phi) \\
 &= \text{tr}(\mathbf{C}_n \Phi),
 \end{aligned} \tag{1.16}$$

where $\mathbf{M}_n \triangleq [\mathbf{V}_n^H, \mathbf{h}_{D,n}]^H \in \mathbb{C}^{(L+1) \times M}$, t' is an auxiliary variable with unit modulus, $\bar{\phi} \triangleq [\phi^H, t']^H \in \mathbb{C}^{(L+1) \times 1}$, $\Phi \triangleq \bar{\phi} \bar{\phi}^H \in \mathbb{C}^{(L+1) \times (L+1)}$, $\mathbf{C}_n \triangleq \mathbf{M}_n \mathbf{w}_{I,n} \mathbf{w}_{I,n}^H \mathbf{M}_n^H \in \mathbb{C}^{(L+1) \times (L+1)}$. On the other hand, we define $t_{I/P,k}$ as

$$\begin{aligned}
 t_{I/P,k} &\triangleq \mathbf{h}^H \mathbf{W}_{I/P,k} \mathbf{h} \\
 &= \text{tr}(\mathbf{h} \mathbf{h}^H \mathbf{W}_{I/P,k}) \\
 &= \text{tr}((\mathbf{h}_D + \mathbf{V}^H \phi) (\mathbf{h}_D^H + \phi^H \mathbf{V}) \mathbf{W}_{I/P,k}) \\
 &= \text{tr}(\mathbf{M}^H \Phi \mathbf{M} \mathbf{W}_{I/P,k}) \\
 &= \text{tr}(\mathbf{M} \mathbf{W}_{I/P,k} \mathbf{M}^H \Phi) \\
 &= \text{tr}(\mathbf{C}_{I/P,k} \Phi),
 \end{aligned} \tag{1.17}$$

where $\mathbf{V} \triangleq [\mathbf{V}_1, \dots, \mathbf{V}_N] \in \mathbb{C}^{L \times MN}$, $\mathbf{M} \triangleq [\mathbf{V}^H, \mathbf{h}_D]^H \in \mathbb{C}^{(L+1) \times MN}$, $\mathbf{C}_{I/P,k} \triangleq \mathbf{M} \mathbf{W}_{I/P,k} \mathbf{M}^H \in \mathbb{C}^{(L+1) \times (L+1)}$. On top of this, (1.7) and (1.9) reduce respectively to

$$R(\Phi) = \sum_{n=1}^N \log_2 \left(1 + \frac{(1-\rho) \text{tr}(\mathbf{C}_n \Phi)}{\sigma_n^2} \right), \tag{1.18}$$

$$\begin{aligned}
 z(\Phi) &= \frac{1}{2} \beta_2 \rho (t_{I,0} + t_{P,0}) + \frac{3}{8} \beta_4 \rho^2 \left(2t_{I,0}^2 + \sum_{k=-N+1}^{N-1} t_{P,k} t_{P,k}^* \right) \\
 &\quad + \frac{3}{2} \beta_4 \rho^2 t_{I,0} t_{P,0}.
 \end{aligned} \tag{1.19}$$

To maximize the non-concave expression (1.19), we successively lower bound the second-order terms by their first-order Taylor expansions [37]. Based on the solution at iteration

$i - 1$, the approximations at iteration i are

$$(t_{I,0}^{(i)})^2 \geq 2t_{I,0}^{(i)}t_{I,0}^{(i-1)} - (t_{I,0}^{(i-1)})^2, \quad (1.20)$$

$$t_{P,k}^{(i)}(t_{P,k}^{(i)})^* \geq 2\Re \left\{ t_{P,k}^{(i)}(t_{P,k}^{(i-1)})^* \right\} - t_{P,k}^{(i-1)}(t_{P,k}^{(i-1)})^*, \quad (1.21)$$

$$t_{I,0}^{(i)}t_{P,0}^{(i)} \geq t_{I,0}^{(i)}t_{P,0}^{(i-1)} + t_{P,0}^{(i)}t_{I,0}^{(i-1)} - t_{I,0}^{(i-1)}t_{P,0}^{(i-1)}. \quad (1.22)$$

Note that $t_{I/P,0} = \text{tr}(\mathbf{C}_{I/P,0}\mathbf{\Phi})$ is real-valued because $\mathbf{C}_{I/P,0}$ and $\mathbf{\Phi}$ are Hermitian matrices. Due to symmetry [36], we have

$$\sum_{k=-N+1}^{N-1} \Re \left\{ t_{P,k}^{(i)}(t_{P,k}^{(i-1)})^* \right\} = \sum_{k=-N+1}^{N-1} t_{P,k}^{(i)}(t_{P,k}^{(i-1)})^*. \quad (1.23)$$

Plugging (1.20)–(1.23) into (1.19), we obtain the DC approximation \tilde{z} as (1.24) and transform problem (1.15) to

$$\max_{\mathbf{\Phi}} \quad \tilde{z}(\mathbf{\Phi}) \quad (1.25a)$$

$$\text{s.t.} \quad R(\mathbf{\Phi}) \geq \bar{R}, \quad (1.25b)$$

$$\text{diag}^{-1}(\mathbf{\Phi}) = \mathbf{1}, \quad (1.25c)$$

$$\mathbf{\Phi} \succeq \mathbf{0}, \quad (1.25d)$$

$$\text{rank}(\mathbf{\Phi}) = 1. \quad (1.25e)$$

We then apply Semi-Definite Relaxation (SDR) to the unit-rank constraint (1.25e) and formulate a Semi-Definite Programming (SDP) with approximation accuracy no greater than $\pi/4$ [38]. In this specific case, we found the solution provided by CVX toolbox [39] to (1.25a)–(1.25d) is always rank-1. This conclusion is summarized below.

Proposition 1. *Any optimal solution $\mathbf{\Phi}^*$ to the relaxed passive beamforming problem (1.25a)–(1.25d) is rank-1 such that (1.25e) is tight and no loss is introduced by SDR.*

In summary, we update $\mathbf{\Phi}^{(i)}$ until convergence, extract $\hat{\phi}^*$ by eigen decomposition, and retrieve the RIS vector by $\phi^* = e^{j \arg([\hat{\phi}^*]_{(1:L)} / [\hat{\phi}^*]_{(L+1)})}$. The passive beamforming design is

$$\begin{aligned} \tilde{z}(\mathbf{\Phi}^{(i)}) = & \frac{1}{2}\beta_2\rho(t_{I,0}^{(i)} + t_{P,0}^{(i)}) + \frac{3}{8}\beta_4\rho^2 \left(4t_{I,0}^{(i)}t_{I,0}^{(i-1)} - 2(t_{I,0}^{(i-1)})^2 + \sum_{k=-N+1}^{N-1} 2t_{P,k}^{(i)}(t_{P,k}^{(i-1)})^* - t_{P,k}^{(i-1)}(t_{P,k}^{(i-1)})^* \right) \\ & + \frac{3}{2}\beta_4\rho^2 \left(t_{I,0}^{(i)}t_{P,0}^{(i-1)} + t_{P,0}^{(i)}t_{I,0}^{(i-1)} - t_{I,0}^{(i-1)}t_{P,0}^{(i-1)} \right). \end{aligned} \quad (1.24)$$

Algorithm 1 SCA: RIS Phase Shift.

- 1: **Input** $\beta_2, \beta_4, \mathbf{h}_{D,n}, \mathbf{V}_n, \sigma_n, \mathbf{w}_{I/P,n}, \rho, \bar{R}, \epsilon, \forall n$
 - 2: Construct $\mathbf{V}, \mathbf{M}, \mathbf{M}_n, \mathbf{C}_n, \mathbf{C}_{I/P,k}, \forall n, k$
 - 3: **Initialize** $i \leftarrow 0, \Phi^{(0)}$
 - 4: Set $t_{I/P,k}^{(0)}, \forall k$ by (1.17)
 - 5: Compute $z^{(0)}$ by (1.19)
 - 6: **Repeat**
 - 7: $i \leftarrow i + 1$
 - 8: Get $\Phi^{(i)}$ by solving (1.25a)–(1.25d)
 - 9: Update $t_{I/P,k}^{(i)}, \forall k$ by (1.17)
 - 10: Compute $z^{(i)}$ by (1.19)
 - 11: **Until** $|z^{(i)} - z^{(i-1)}| \leq \epsilon$
 - 12: Set $\Phi^* \leftarrow \Phi^{(i)}$
 - 13: Get $\hat{\phi}^*$ by eigen decomposition, $\Phi^* = \hat{\phi}^* (\hat{\phi}^*)^H$
 - 14: Set $\phi^* \leftarrow e^{j \arg([\hat{\phi}^*]_{(1:L)} / [\hat{\phi}^*]_{(L+1)})}$
 - 15: **Output** ϕ^*
-

summarized in the SCA Algorithm 1, where the relaxed problem (1.25a)–(1.25d) involves a $(L + 1)$ -order positive semi-definite matrix variable and $(L + 2)$ linear constraints. Given a solution accuracy ϵ_{IPM} for the interior-point method, the computational complexity of Algorithm 1 is $\mathcal{O}(I_{\text{SCA}}(L + 2)^4(L + 1)^{0.5} \log(\epsilon_{\text{IPM}}^{-1}))$, where I_{SCA} denotes the number of SCA iterations [38].

Proposition 2. *For any feasible initial point with given waveform and splitting ratio, the SCA Algorithm 1 is guaranteed to converge to local optimal points of the original problem (1.15).*

1.3.2 Active Beamforming

The original waveform and active beamforming problem (1.15) is over complex vectors $\mathbf{w}_{I/P}$ of size $MN \times 1$. Next, we decouple the design in spatial and frequency domains, enable independent optimizations correspondingly, and reduce the size of variables from $2MN$ to $2(M + N)$. The weight on subband n is essentially

$$\mathbf{w}_{I/P,n} = s_{I/P,n} \mathbf{b}_{I/P,n}, \quad (1.26)$$

where $s_{I/P,n}$ denotes the amplitude of the modulated/multisine waveform at tone n , and $\mathbf{b}_{I/P,n}$ denotes the corresponding information/power precoder. Define $\mathbf{s}_{I/P} \triangleq [s_{I/P,1}, \dots, s_{I/P,N}]^T \in$

$\mathbb{R}_+^{N \times 1}$. The MRT precoder at subband n is given by

$$\mathbf{b}_{\text{I/P},n}^* = \frac{\mathbf{h}_n}{\|\mathbf{h}_n\|}. \quad (1.27)$$

Proposition 3. *For single-user SWIPT, the global optimal information and power precoders coincide at the MRT.*

1.3.3 Waveform and Splitting Ratio

Next, we jointly optimize the waveform amplitude $\mathbf{s}_{\text{I/P}}$ and the splitting ratio ρ for any given RIS phase shift ϕ and active precoder $\mathbf{b}_{\text{I/P},n}, \forall n$. On top of (1.27), the equivalent channel strength at subband n is $\|\mathbf{h}_n\|$. Hence, the rate (1.7) reduces to

$$R(\mathbf{s}_{\text{I}}, \rho) = \log_2 \prod_{n=1}^N \left(1 + \frac{(1-\rho)\|\mathbf{h}_n\|^2 s_{\text{I},n}^2}{\sigma_n^2} \right), \quad (1.28)$$

and the DC (1.9) rewrites as (1.29), so that problem (1.15) boils down to

$$\max_{\mathbf{s}_{\text{I}}, \mathbf{s}_{\text{P}}, \rho} z(\mathbf{s}_{\text{I}}, \mathbf{s}_{\text{P}}, \rho) \quad (1.30a)$$

$$\text{s.t.} \quad R(\mathbf{s}_{\text{I}}, \rho) \geq \bar{R}, \quad (1.30b)$$

$$\frac{1}{2} (\|\mathbf{s}_{\text{I}}\|^2 + \|\mathbf{s}_{\text{P}}\|^2) \leq P. \quad (1.30c)$$

$$\begin{aligned} z(\mathbf{s}_{\text{I}}, \mathbf{s}_{\text{P}}, \rho) = & \frac{1}{2} \beta_2 \rho \sum_{n=1}^N \|\mathbf{h}_n\|^2 (s_{\text{I},n}^2 + s_{\text{P},n}^2) + \frac{3}{8} \beta_4 \rho^2 \left(2 \sum_{n_1, n_2} \prod_{j=1}^2 \|\mathbf{h}_{n_j}\|^2 s_{\text{I},n_j}^2 + \sum_{\substack{n_1, n_2, n_3, n_4 \\ n_1 + n_2 = n_3 + n_4}} \prod_{j=1}^4 \|\mathbf{h}_{n_j}\| s_{\text{P},n_j} \right) \\ & + \frac{3}{2} \beta_4 \rho^2 \left(\sum_{n_1, n_2} \|\mathbf{h}_{n_1}\|^2 \|\mathbf{h}_{n_2}\|^2 s_{\text{I},n_1}^2 s_{\text{P},n_2}^2 \right). \end{aligned} \quad (1.29)$$

Following [14], we introduce auxiliary variables t'' , $\bar{\rho}$ and transform problem (1.30) into a reversed GP

$$\min_{\mathbf{s}_I, \mathbf{s}_P, \rho, \bar{\rho}, t''} \quad \frac{1}{t''} \quad (1.31a)$$

$$\text{s.t.} \quad \frac{t''}{z(\mathbf{s}_I, \mathbf{s}_P, \rho)} \leq 1, \quad (1.31b)$$

$$\frac{2^{\bar{R}}}{\prod_{n=1}^N (1 + \bar{\rho} \|\mathbf{h}_n\|^2 s_{I,n}^2 / \sigma_n^2)} \leq 1, \quad (1.31c)$$

$$\frac{1}{2} (\|\mathbf{s}_I\|^2 + \|\mathbf{s}_P\|^2) \leq P, \quad (1.31d)$$

$$\rho + \bar{\rho} \leq 1. \quad (1.31e)$$

It can be concluded that $\bar{\rho}^* = 1 - \rho^*$ as no power is wasted at the receiver. The denominators of (1.31c) and (1.31b) consist of posynomials [40] that can be decomposed as sums of monomials

$$1 + \frac{\bar{\rho} \|\mathbf{h}_n\|^2 s_{I,n}^2}{\sigma_n^2} \triangleq \sum_{m_{I,n}} g_{m_{I,n}}(s_{I,n}, \bar{\rho}), \quad (1.32)$$

$$z(\mathbf{s}_I, \mathbf{s}_P, \rho) \triangleq \sum_{m_P} g_{m_P}(\mathbf{s}_I, \mathbf{s}_P, \rho). \quad (1.33)$$

We upper bound (1.32) and (1.33) by the Geomtric Mean (GM)-Arithmetic Mean (AM) inequality [41] and transform problem (1.31) to

$$\min_{\mathbf{s}_I, \mathbf{s}_P, \rho, \bar{\rho}, t''} \quad \frac{1}{t''} \quad (1.34a)$$

$$\text{s.t.} \quad t'' \prod_{m_P} \left(\frac{g_{m_P}(\mathbf{s}_I, \mathbf{s}_P, \rho)}{\gamma_{m_P}} \right)^{-\gamma_{m_P}} \leq 1, \quad (1.34b)$$

$$2^{\bar{R}} \prod_n \prod_{m_{I,n}} \left(\frac{g_{m_{I,n}}(s_{I,n}, \bar{\rho})}{\gamma_{m_{I,n}}} \right)^{-\gamma_{m_{I,n}}} \leq 1, \quad (1.34c)$$

$$\frac{1}{2} (\|\mathbf{s}_I\|^2 + \|\mathbf{s}_P\|^2) \leq P, \quad (1.34d)$$

$$\rho + \bar{\rho} \leq 1, \quad (1.34e)$$

Algorithm 2 GP: Waveform Amplitude and Splitting Ratio.

```

1: Input  $\beta_2, \beta_4, \mathbf{h}_n, P, \sigma_n, \bar{R}, \epsilon, \forall n$ 
2: Initialize  $i \leftarrow 0, \mathbf{s}_{I/P}^{(0)}, \rho^{(0)}$ 
3: Compute  $R^{(0)}, z^{(0)}$  by (1.28), (1.29)
4: Set  $g_{m_{I,n}}^{(0)}, g_{m_P}^{(0)}, \forall n$  by (1.32), (1.33)
5: Repeat
6:    $i \leftarrow i + 1$ 
7:   Update  $\gamma_{m_{I,n}}^{(i)}, \gamma_{m_P}^{(i)}, \forall n$  by (1.35), (1.36)
8:   Get  $\mathbf{s}_{I/P}^{(i)}, \rho^{(i)}$  by solving problem (1.34)
9:   Compute  $R^{(i)}, z^{(i)}$  by (1.28), (1.29)
10:  Update  $g_{m_{I,n}}^{(i)}, g_{m_P}^{(i)}, \forall n$  by (1.32), (1.33)
11: Until  $|z^{(i)} - z^{(i-1)}| \leq \epsilon$ 
12: Set  $\mathbf{s}_{I/P}^* \leftarrow \mathbf{s}_{I/P}^{(i)}, \rho^* \leftarrow \rho^{(i)}$ 
13: Output  $\mathbf{s}_I^*, \mathbf{s}_P^*, \rho^*$ 

```

where $\gamma_{m_{I,n}}, \gamma_{m_P} \geq 0$ and $\sum_{m_{I,n}} \gamma_{m_{I,n}} = \sum_{m_P} \gamma_{m_P} = 1$. The tightness of the AM-GM inequality depends on $\{\gamma_{m_{I,n}}, \gamma_{m_P}\}$, and a feasible choice at iteration i is

$$\gamma_{m_{I,n}}^{(i)} = \frac{g_{m_{I,n}}(\mathbf{s}_{I,n}^{(i-1)}, \bar{\rho}^{(i-1)})}{1 + \bar{\rho}^{(i-1)} \|\mathbf{h}_n\|^2 (\mathbf{s}_{I,n}^{(i-1)})^2 / \sigma_n^2}, \quad (1.35)$$

$$\gamma_{m_P}^{(i)} = \frac{g_{m_P}(\mathbf{s}_I^{(i-1)}, \mathbf{s}_P^{(i-1)}, \rho^{(i-1)})}{z(\mathbf{s}_I^{(i-1)}, \mathbf{s}_P^{(i-1)}, \rho^{(i-1)})}. \quad (1.36)$$

With (1.35) and (1.36), problem (1.34) can be solved by existing optimization tools such as CVX toolbox [39]. We update $\mathbf{s}_I^{(i)}, \mathbf{s}_P^{(i)}, \rho^{(i)}$ iteratively until convergence. The joint waveform amplitude and splitting ratio design is summarized in the GP Algorithm 2, which achieves local optimality at the cost of exponential computational complexity [41].

Proposition 4. *For any feasible initial point, the GP Algorithm 2 is guaranteed to converge to local optimal points of the waveform amplitude and splitting ratio design problem (1.30).*

Proof. Please refer to [8, 14]. □

1.3.4 Low-Complexity Adaptive Design

To facilitate practical SWIPT implementation, we propose two closed-form adaptive waveform amplitude schemes by combining WF and SMF in time and power domains, respectively. For

WIT, the optimal WF strategy assigns the amplitude of modulated tone n by

$$s_{I,n} = \sqrt{2 \left(\lambda - \frac{\sigma_n^2}{P \|\mathbf{h}_n\|^2} \right)^+}, \quad (1.37)$$

where λ is chosen to satisfy the power constraint $\|\mathbf{s}_I\|^2/2 \leq P$. The closed-form solution can be obtained by iterative power allocation [42], and the details are omitted here. On the other hand, SMF was proposed in [12] as a suboptimal WPT resource allocation scheme that assigns the amplitude of sinewave n by

$$s_{P,n} = \sqrt{\frac{2P}{\sum_{n=1}^N \|\mathbf{h}_n\|^{2\alpha}}} \|\mathbf{h}_n\|^\alpha, \quad (1.38)$$

where the scaling ratio $\alpha \geq 1$ is predetermined to exploit the rectifier nonlinearity and frequency selectivity. When the receiver works in TS mode, there is no superposition in the suboptimal waveform design (modulated waveform with amplitude (1.37) is used in the data session while multisine waveform with amplitude (1.38) is used in the energy session). When the receiver works in PS mode, we jointly design the combining ratio δ with the splitting ratio ρ , and assign the superposed waveform amplitudes as

$$s_{I,n} = \sqrt{2(1-\delta) \left(\lambda - \frac{\sigma_n^2}{P \|\mathbf{h}_n\|^2} \right)^+}, \quad (1.39)$$

$$s_{P,n} = \sqrt{\frac{2\delta P}{\sum_{n=1}^N \|\mathbf{h}_n\|^{2\alpha}}} \|\mathbf{h}_n\|^\alpha, \quad (1.40)$$

where the δ determines the power ratio of multisine waveform at the transmitter, and ρ determines the power ratio of the energy harvester at the receiver.⁵

Besides, minor modifications are required for passive beamforming to accommodate the low-complexity waveform schemes. Specifically, the rate constraint (1.25b) should be dropped as the achievable rate is controlled by η or $\{\delta, \rho\}$. To achieve the WIT point ($\rho = 0$), the rate (1.18) should be maximized, the current expression (1.24) is not needed and no SCA is involved. The Modified-SCA (M-SCA) Algorithm 3 summarizes the modified passive beamforming design when the receiver works in PS mode. Similarly, no loss is introduced by SDR and local optimality is guaranteed. The proofs are omitted here. Since each SDP involves $(L + 1)$ linear constraints, the computational complexity of Algorithm 3

⁵We notice that $\delta^* = \rho^* = 0$ at the WIT point and $\delta^* = \rho^* = 1$ at the WPT point when N is relatively large. Intuitively, δ^* and ρ^* should be positively correlated for efficient SWIPT design.

Algorithm 3 M-SCA: RIS Phase Shift.

```

1: Input  $\beta_2, \beta_4, \mathbf{h}_{D,n}, \mathbf{V}_n, \sigma_n, \mathbf{w}_{I/P,n}, \rho, \epsilon, \forall n$ 
2: Construct  $\mathbf{V}, \mathbf{M}, \mathbf{M}_n, \mathbf{C}_n, \mathbf{C}_{I/P,k}, \forall n, k$ 
3: Initialize  $i \leftarrow 0, \Phi^{(0)}$ 
4: If  $\rho = 0$ 
5:   Get  $\Phi^*$  by maximizing (1.18) s.t. (1.25c), (1.25d)
6: Else
7:   Set  $t_{I/P,k}^{(0)}, \forall k$  by (1.17)
8:   Compute  $z^{(0)}$  by (1.19)
9:   Repeat
10:     $i \leftarrow i + 1$ 
11:    Get  $\Phi^{(i)}$  by maximizing (1.24) s.t. (1.25c), (1.25d)
12:    Update  $t_{I/P,k}^{(i)}, \forall k$  by (1.17)
13:    Compute  $z^{(i)}$  by (1.19)
14:  Until  $|z^{(i)} - z^{(i-1)}| \leq \epsilon$ 
15:  Set  $\Phi^* \leftarrow \Phi^{(i)}$ 
16: End If
17: Get  $\hat{\phi}^*$  by eigen decomposition,  $\Phi^* = \hat{\phi}^* (\hat{\phi}^*)^H$ 
18: Set  $\phi^* \leftarrow e^{j \arg([\hat{\phi}^*]_{(1:L)} / [\hat{\phi}^*]_{(L+1)})}$ 
19: Output  $\phi^*$ 

```

is $\mathcal{O}(I_{\text{M-SCA}}(L+1)^{4.5} \log(\epsilon_{\text{IPM}}^{-1}))$, where $I_{\text{M-SCA}}$ denotes the number of M-SCA iterations [38]. Note that no SCA is involved at the WIT point where $I_{\text{M-SCA}} = 1$.

1.3.5 Block Coordinate Descent

Based on the direct and cascaded CSIT, we iteratively update the passive beamforming ϕ by Algorithm 1, the active precoder $\mathbf{b}_{I/P,n}, \forall n$ by equation (1.27), and the waveform amplitude $s_{I/P}$ and splitting ratio ρ by Algorithm 2, until convergence. The steps are summarized in the BCD Algorithm 4, whose computational complexity is exponential as inherited from Algorithm 2. It is guaranteed to converge, but may end up with a suboptimal solution because variables are coupled in constraint (1.15b) [43].

For the low-complexity design under PS mode, we obtain the phase shift by Algorithm 3, the active precoder $\mathbf{b}_{I/P,n}, \forall n$ by equation (1.27), and the waveform amplitude by (1.39) and (1.40). To achieve the WIT point ($\rho = 0$), the rate (1.18) should be maximized to obtain the maximum capacity C_{\max} .⁶ Note that the BCD algorithm obtains the R-E region by varying the rate constraint from 0 to C_{\max} , while the achievable R-E region of the Low-Complexity (LC)-BCD algorithm can be obtained by performing a two-dimensional search over (δ, ρ) from

⁶Recall in Remark 2 that different subchannel designs lead to different capacities.

Algorithm 4 BCD: Waveform, Beamforming and Splitting Ratio.

- 1: **Input** $\beta_2, \beta_4, \mathbf{h}_{D,n}, \mathbf{V}_n, P, \sigma_n, \bar{R}, \epsilon, \forall n$
 - 2: **Initialize** $i \leftarrow 0, \phi^{(0)}, \mathbf{b}_{I/P,n}^{(0)}, \mathbf{s}_{I/P}^{(0)}, \rho^{(0)}, \forall n$
 - 3: Set $\mathbf{w}_{I/P,n}^{(0)}, \forall n$ by (1.26)
 - 4: Compute $z^{(0)}$ by (1.29)
 - 5: **Repeat**
 - 6: $i \leftarrow i + 1$
 - 7: Get $\phi^{(i)}$ based on $\mathbf{w}_{I/P}^{(i-1)}, \rho^{(i-1)}$ by Algorithm 1
 - 8: Update $\mathbf{h}_n^{(i)}, \mathbf{b}_n^{(i)}, \forall n$ by (1.5), (1.27)
 - 9: Get $\mathbf{s}_{I/P}^{(i)}, \rho^{(i)}$ by Algorithm 2
 - 10: Update $\mathbf{w}_{I/P,n}^{(i)}, \forall n$ by (1.26)
 - 11: Compute $z^{(i)}$ by (1.29)
 - 12: **Until** $|z^{(i)} - z^{(i-1)}| \leq \epsilon$
 - 13: Set $\phi^* \leftarrow \phi^{(i)}, \mathbf{w}_{I/P}^* \leftarrow \mathbf{w}_{I/P}^{(i)}, \rho^* \leftarrow \rho^{(i)}$
 - 14: **Output** $\phi^*, \mathbf{w}_I^*, \mathbf{w}_P^*, \rho^*$
-

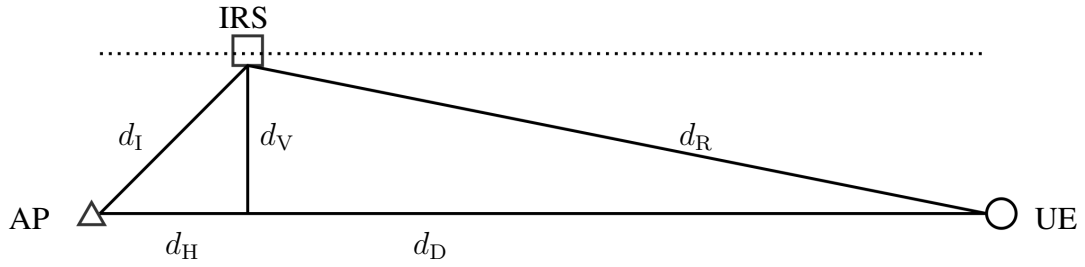


Fig. 1.5 System layout in simulation.

$(0, 0)$ to $(1, 1)$. The steps are summarized in Algorithm 5. The computational complexity of Algorithm 5 is $\mathcal{O}(I_{\text{LC-BCD}} I_{\text{M-SCA}} (L + 1)^{4.5} \log(\epsilon_{\text{IPM}}^{-1}))$, where $I_{\text{LC-BCD}}$ denotes the number of LC-BCD iterations [38].

1.4 Performance Evaluations

To evaluate the proposed RIS-aided SWIPT system, we consider the layout in Fig. 1.5 where the RIS moves along a line parallel to the AP-UE path. Let d_H, d_V be the horizontal and vertical distances from the AP to the RIS, and denote respectively $d_D, d_I = \sqrt{d_H^2 + d_V^2}, d_R = \sqrt{(d_D - d_H)^2 + d_V^2}$ as the distance of direct, incident and reflected links. $d_D = 12$ m and $d_H = d_V = 2$ m are chosen as reference. The path loss of direct, incident and reflected links are denoted by Λ_D, Λ_I and Λ_R , respectively. We consider a large open space Wi-Fi-like environment at center frequency 2.4 GHz where the channel follows IEEE TGn channel

Algorithm 5 LC-BCD: Waveform and Beamforming.

```

1: Input  $\beta_2, \beta_4, \mathbf{h}_{D,n}, \mathbf{V}_n, P, \sigma_n, \delta, \rho, \epsilon, \forall n$ 
2: Initialize  $i \leftarrow 0, \phi^{(0)}, \mathbf{b}_{I/P,n}^{(0)}, \mathbf{s}_{I/P}^{(0)}, \forall n$ 
3: Set  $\mathbf{w}_{I/P,n}^{(0)}, \forall n$  by (1.26)
4: Compute  $R^{(0)}, z^{(0)}$  by (1.28), (1.29)
5: Repeat
6:    $i \leftarrow i + 1$ 
7:   Get  $\phi^{(i)}$  based on  $\mathbf{w}_{I/P}^{(i-1)}$  by Algorithm 3
8:   Update  $\mathbf{h}_n^{(i)}, \mathbf{b}_n^{(i)}, \forall n$  by (1.5), (1.27)
9:   Update  $\mathbf{s}_I^{(i)}, \mathbf{s}_P^{(i)}$  by (1.39), (1.40)
10:  Update  $\mathbf{w}_{I/P,n}^{(i)}, \forall n$  by (1.26)
11:  Compute  $R^{(i)}, z^{(i)}$  by (1.28), (1.29)
12:  If  $\rho = 0$ 
13:     $\Delta \leftarrow R^{(i)} - R^{(i-1)}$ 
14:  Else
15:     $\Delta \leftarrow z^{(i)} - z^{(i-1)}$ 
16:  End If
17: Until  $|\Delta| \leq \epsilon$ 
18: Set  $\phi^* \leftarrow \phi^{(i)}, \mathbf{w}_{I/P}^* \leftarrow \mathbf{w}_{I/P}^{(i)}$ 
19: Output  $\phi^*, \mathbf{w}_I^*, \mathbf{w}_P^*$ 

```

model D [44]. Specifically, the path loss exponent is 2 (i.e., free-space model) up to 10 m, and 3.5 onwards to further penalize the channels with large distance. All fading are modeled as Non-Line-of-Sight (LoS) with tap delays and powers specified in model D, and the tap gains are modeled as i.i.d. CSCG variables. Rectenna parameters are set to $k_2 = 0.0034$, $k_4 = 0.3829$, $R_A = 50 \Omega$ [8] such that $\beta_2 = 0.17$ and $\beta_4 = 957.25$. We also choose the average Effective Isotropic Radiated Power (EIRP) as $P = 40$ dBm, the receive antenna gain as 3 dBi, the scaling ratio as $\alpha = 2$, and the tolerance as $\epsilon = 10^{-8}$. To further reduce the complexity, we assume $\delta = \rho$ for simplicity and perform a one-dimensional search from 0 to 1 to obtain an inner R-E bound for the LC-BCD algorithm. Each R-E point is averaged over 200 channel realizations, and the x -axis is normalized to per-subband rate R/N .

Fig. 1.6 reveals how RIS influences the sorted equivalent subchannel amplitude for one channel realization. Due to the flexible subchannel design enabled by passive beamforming, the optimal amplitude distribution for WIT and WPT are dissimilar. Under the specified configuration, the WPT-optimized RIS aligns the strong subbands to exploit the rectifier nonlinearity. On the other hand, the WIT-optimized RIS provides a fair gain over all subchannels when L is sufficiently large. This is reminiscent of the WF scheme at high SNR, but is realized by channel alignment instead of resource allocation. Nevertheless, the

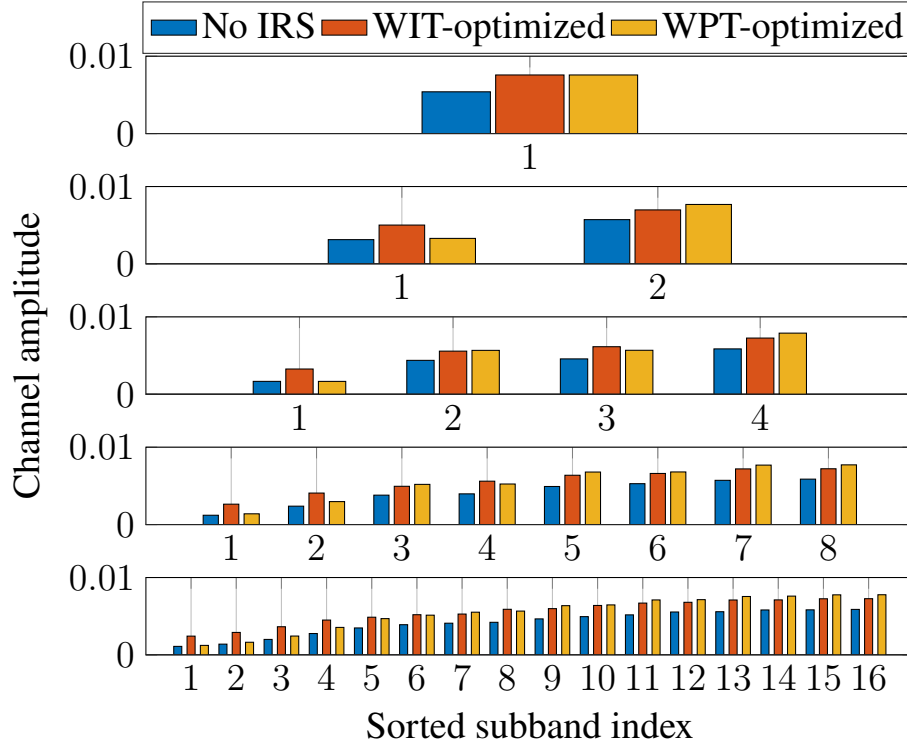


Fig. 1.6 Sorted equivalent subchannel amplitude with and without RIS versus N for $M = 1$, $L = 100$, $\sigma_n^2 = -40$ dBm, $B = 10$ MHz and $d_H = d_V = 2$ m.

amplitude of modulated and multisine waveforms remains approximately unchanged when adding a RIS (the plots are not attached). In other words, RIS has a subtle impact on the waveform design.

Fig. 1.7(a) illustrates the average R-E region versus the number of subband N . First, it is observed that increasing N reduces the per-subband rate but boosts the harvested energy. This is because less power is allocated to each subband but more balanced DC terms are introduced by frequency coupling to boost the harvested energy. On the other hand, Fig. 1.7(b) presents the sorted modulated/multisine amplitude $s_{I/P}$ for WPT. It demonstrates that a dedicated multisine waveform is unnecessary for a small N but is required for a large N . This observation originates from the rectifier nonlinearity. Although both waveforms have equivalent second-order DC terms (1.10) and (1.12), for the fourth-order terms (1.11) and (1.13), the modulated waveform has N^2 monomials with a modulation gain of 2, while the multisine has $(2N^3 + N)/3$ monomials as the components of different frequencies compensate and produce DC. Second, the R-E region is convex for $N \in \{2, 4\}$ and concave-convex for $N \in \{8, 16\}$, such that PS outperforms TS for a small N and is outperformed for a large N . When N is in between, the optimal strategy is a combination of both, i.e., a time sharing between the WPT point and the saddle PS SWIPT point (as denoted by the red curve in Fig. 1.7(a)). When

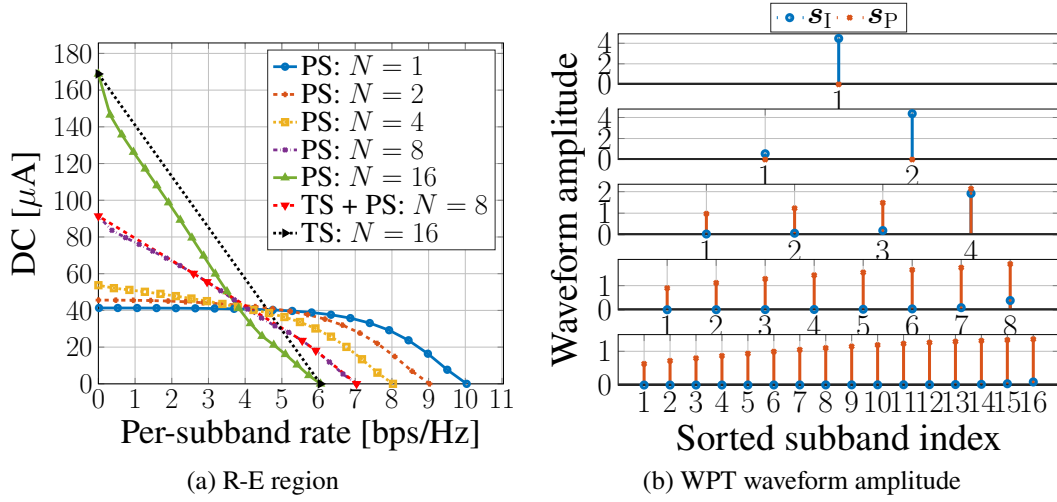


Fig. 1.7 Average R-E region and WPT waveform amplitude versus N for $M = 1$, $L = 20$, $\sigma_n^2 = -40$ dBm, $B = 1$ MHz and $d_H = d_V = 2$ m.

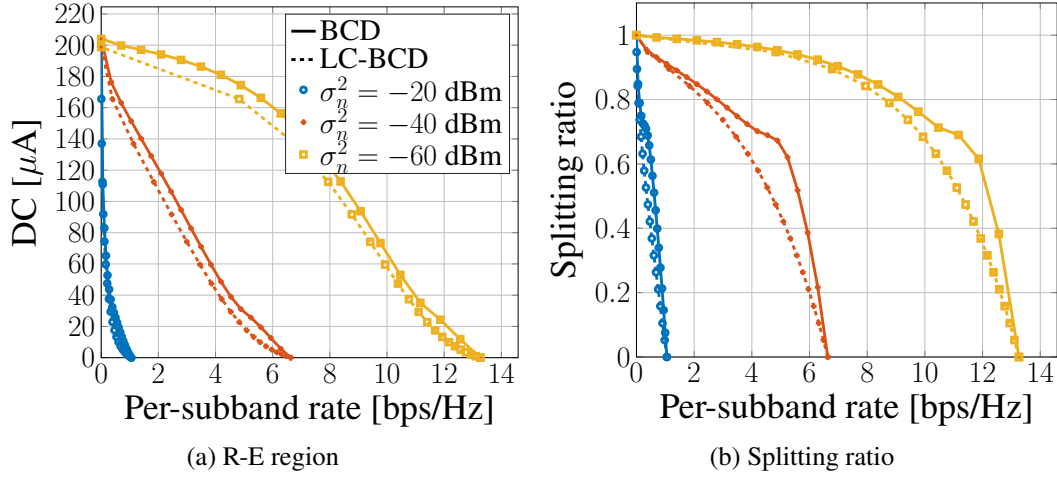


Fig. 1.8 Average R-E region and splitting ratio versus σ_n^2 for $M = 1$, $N = 16$, $L = 20$, $B = 1$ MHz and $d_H = d_V = 2$ m.

N is relatively small, only modulated waveform is used at both WIT and WPT points, and one can infer that no multisine waveform is needed for the entire R-E region. It aligns with the conclusion based on the conventional linear harvester model, namely the R-E region is convex, PS outperforms TS, and dedicated power waveform is unnecessary. As N becomes sufficiently large, the multisine waveform further boosts WPT and creates some concavity in the high-power region, which accounts for the superiority of TS under the nonlinear harvester model. Therefore, we conclude that the rectifier nonlinearity enlarges the R-E region by favoring a different waveform and receiving mode, both heavily depending on N .

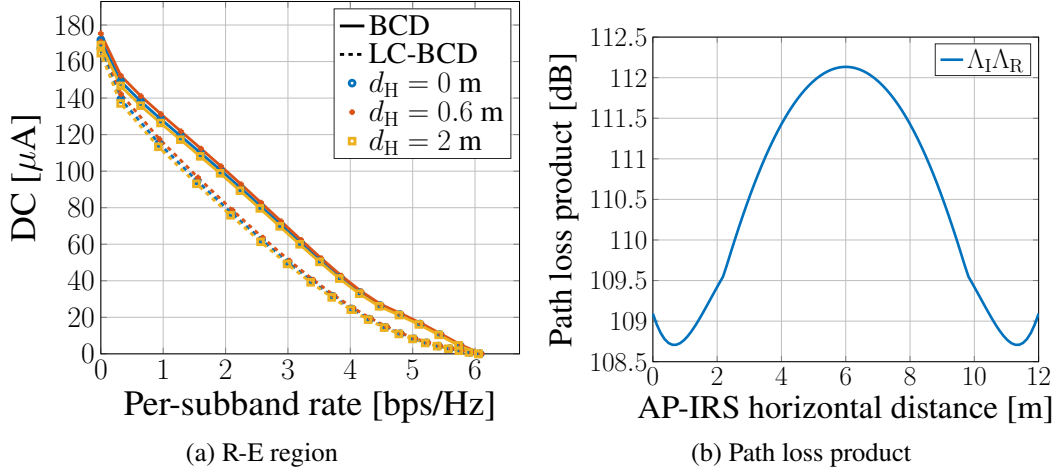


Fig. 1.9 Average R-E region and path loss versus d_H for $M = 1$, $N = 16$, $L = 20$, $\sigma_n^2 = -40$ dBm, $B = 1$ MHz and $d_V = 2$ m.

The average noise power influences the R-E region as shown in Fig. 1.8(a). First, we note that the R-E region is roughly concave/convex at low/high SNR such that TS/PS are preferred correspondingly. At low SNR, the power is allocated to the modulated waveform on a few strongest subbands to achieve a high rate. As the rate constraint \bar{R} decreases, Algorithm 2 activates more subbands that further boosts the harvested DC power because of frequency coupling and harvester nonlinearity. Second, there exists a turning point in the R-E region, especially for a low noise level ($\sigma_n^2 \leq -40$ dBm). The reason is that when \bar{R} departs slightly from the maximum value, the algorithm tends to adjust the splitting ratio ρ rather than allocate more power to the multisine waveform, since a small amplitude multisine could be inefficient for energy purpose. As \bar{R} further decreases, thanks to the advantage of multisine, a superposed waveform with a small ρ can outperform a modulated waveform with a large ρ . The result proves the benefit of superposed waveform and the necessity of joint waveform and splitting ratio optimization. Besides, the LC-BCD algorithm achieves a good balance between performance and complexity even if one-dimensional search is considered for $\delta = \rho$ from 0 to 1.

In Fig. 1.9(a), we compare the average R-E region achieved by different AP-RIS horizontal distance d_H . Different from the active Amplify-and-Forward (AF) relay that favors midpoint development [45], the RIS should be placed close to either the AP or the UE based on the product path loss model that applies to finite-size element reflection [46, 47]. Moreover, there exist two optimal RIS coordinates around $d_H = 0.6$ and 11.4 m that minimize the path loss product $\Lambda_I \Lambda_R$ and maximize the R-E tradeoff. It suggests that equipping the AP with a RIS can potentially extend the operation range of SWIPT systems.

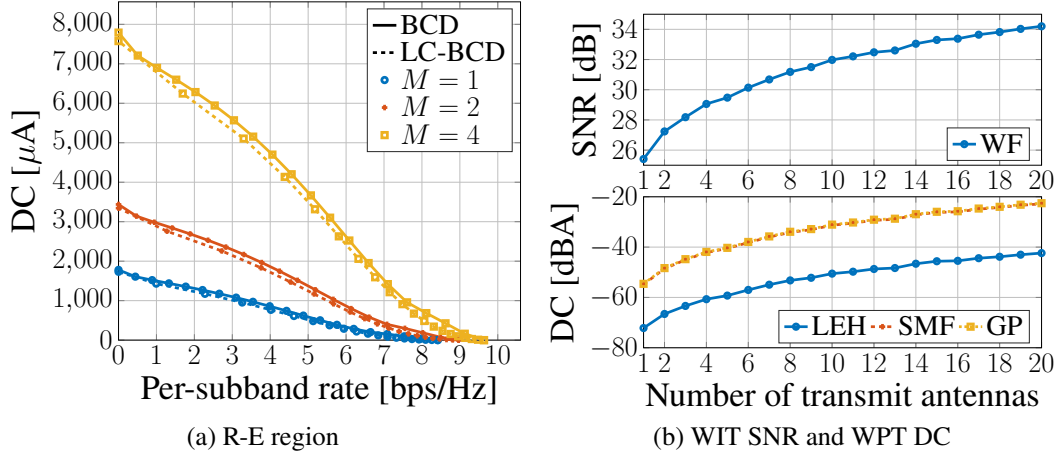


Fig. 1.10 Average R-E region, WIT SNR and WPT DC versus M for $N = 16$, $L = 20$, $\sigma_n^2 = -40$ dBm, $B = 1$ MHz, $d_H = d_V = 0.2$ m.

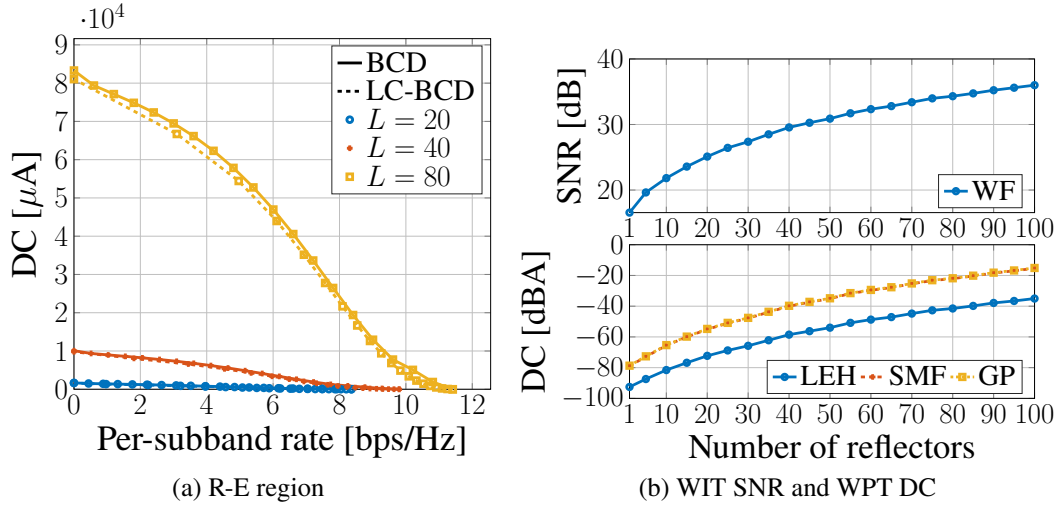


Fig. 1.11 Average R-E region, WIT SNR and WPT DC versus L for $M = 1$, $N = 16$, $\sigma_n^2 = -40$ dBm, $B = 1$ MHz and $d_H = d_V = 0.2$ m.

The impacts of the number of transmit antennas M and the RIS elements L on the R-E behavior are revealed in Figs. 1.10(a) and 1.11(a). First, it is observed that adding either active or passive elements can improve the equivalent SNR, which produces a nearly concave R-E region and favors the PS receiver. Second, the conventional Linear Energy Harvester (LEH) model leads to a power-inefficient design. To investigate the performance loss, we truncate the DC objective function (1.8) at $n_0 = 2$ such that (i) in the passive beamforming problem, $z(\Phi) = \beta_2 \rho(t_{I,0} + t_{P,0})/2$ and no SCA is required; (ii) in the waveform design problem, the WPT-optimal strategy is the adaptive single sinewave that allocates all power to the multisine at the strongest subband [8]. As shown in Figs. 1.10(b) and 1.11(b), those

conventional designs do not exploit the harvester nonlinearity and end up with a nearly 20 dBA gap compared to the nonlinear model-based SMF and GP designs. Third, doubling M brings a 3 dB gain at the output SNR and a 12 dBA increase at the harvested DC, which verified that active beamforming has an array gain of M [42] with power scaling order M^2 under the truncated nonlinear harvester model [8, 14]. Fourth, when the RIS is very close to the AP or UE, doubling L can bring a 6 dB gain at the output SNR and a 24 dBA increase at the harvested DC. From the perspective of WIT, it suggests that passive beamforming can reach an array gain of L^2 , as indicated by [23]. An interpretation is that the RIS coherently combines the incoming signal with a receive array gain L , then performs an equal gain reflection with a transmit array gain L . From the perspective of WPT, it suggests that passive beamforming comes with a power scaling order L^4 under the truncated nonlinear harvester model. We then verify this novel observation in a simplified case where the power is uniformly allocated over multisine, all channels are frequency-flat, and L is sufficiently large such that the direct channel becomes negligible. Let X be the cascaded small-scale fading coefficient. The DC in such case reduces to

$$z = \beta_2 \Lambda_R^2 \Lambda_I^2 |X|^2 L^2 P + \beta_4 \frac{2N^2 + 1}{2N} \Lambda_R^4 \Lambda_I^4 |X|^4 L^4 P^2, \quad (1.41)$$

which scales quartically with L . Compared with active antennas, RIS elements achieve higher array gain and power scaling order, but a very large L is required to compensate the double fading of the auxiliary link. These observations demonstrate the R-E benefit of passive beamforming and emphasize the importance of accounting for the harvester nonlinearity in the waveform and beamforming design.

Figs. 1.12(a) and 1.12(b) explore the R-E region with different RIS strategies for narrowband and broadband SWIPT. The ideal Frequency-Selective (FS) RIS assumes the reflection coefficient of each element is independent and controllable at different frequencies. The adaptive RIS adjusts the passive beamforming for different R-E points by Algorithm 1. The WIT/WPT-optimized RIS is retrieved by Algorithm 3 then fixed for the whole R-E region. The random RIS models the phase shift of all elements as i.i.d. uniform random variables over $[0, 2\pi)$. First, random RIS and no RIS perform worse than other schemes since no passive beamforming is exploited. Their R-E boundaries coincide as the antenna mode reflection of the random RIS is canceled out after averaging. Second, when the bandwidth is small, the performance of ideal, adaptive, and WIT/WPT-optimized RIS are similar; when the bandwidth is large, the adaptive RIS outperforms the WIT/WPT-optimized RIS but is outperformed by the ideal FS RIS. In the former case, the subband responses are close to each other such that the tradeoff in Remark 2 becomes insignificant, and the auxiliary link can be roughly maximized at all subbands. It suggests that for narrowband SWIPT, the

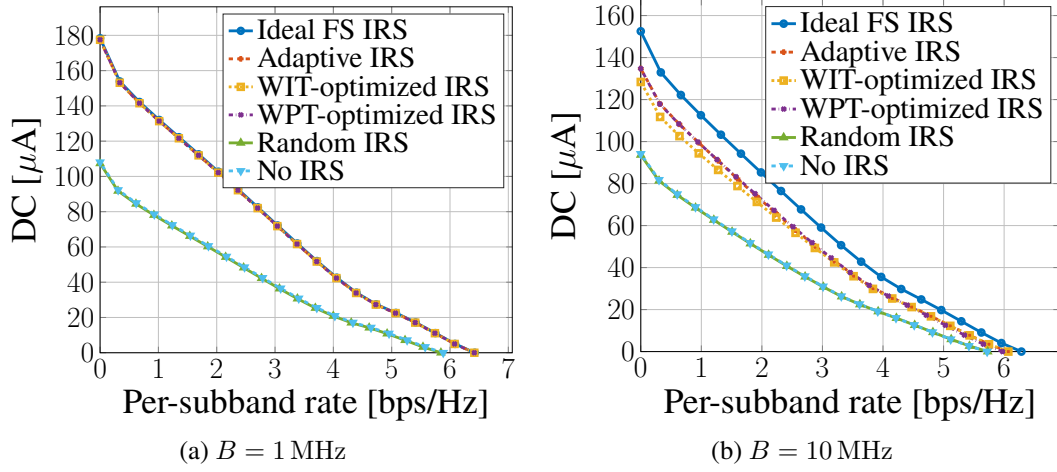


Fig. 1.12 Average R-E region for ideal, adaptive, fixed and no RIS versus B for $M = 1$, $N = 16$, $L = 20$, $\sigma_n^2 = -40$ dBm and $d_H = d_V = 2$ m.

optimal passive beamforming for any R-E point is optimal for the whole R-E region, and the corresponding composite channel and active precoder are also optimal for the whole R-E region. Hence, the achievable R-E region is obtained by optimizing the waveform amplitude and splitting ratio. On the other hand, since the channel frequency selectivity affects the performance of the information decoder and energy harvester differently, the optimal RIS reflection coefficient varies at different R-E tradeoffs points for broadband SWIPT. As shown in Fig. 1.6, the subchannel amplification can be either spread evenly to improve the rate at high SNR, or focused on a few strongest subbands to boost the output DC, thanks to adaptive passive beamforming.

We then explore the impacts of imperfect cascaded CSIT and quantized RIS on the R-E performance. Due to the general lack of RF-chains at the RIS, it can be challenging to acquire accurate cascaded CSIT on a short-term basis. We assume the cascaded channel at subband n is

$$\mathbf{V}_n = \hat{\mathbf{V}}_n + \tilde{\mathbf{V}}_n, \quad (1.42)$$

where $\hat{\mathbf{V}}_n$ is the estimated cascaded CSIT and $\tilde{\mathbf{V}}_n$ is the estimation error with entries following i.i.d. CSCG distribution $\mathcal{CN}(0, \epsilon_n^2)$.⁷ Figure 1.13(a) shows that the proposed passive beamforming Algorithm 1 is robust to cascaded CSIT inaccuracy for broadband SWIPT with different L . On the other hand, since the practical reflection coefficient depends on the available element impedances, we consider a discrete RIS codebook $\mathcal{C}_\phi = \{e^{j2\pi i/2^b} \mid i = 1, \dots, 2^b\}$ and uniformly quantize the continuous reflection coefficients obtained by Algorithm 4 to

⁷Note that the subchannel responses are correlated but the estimations can be independent.

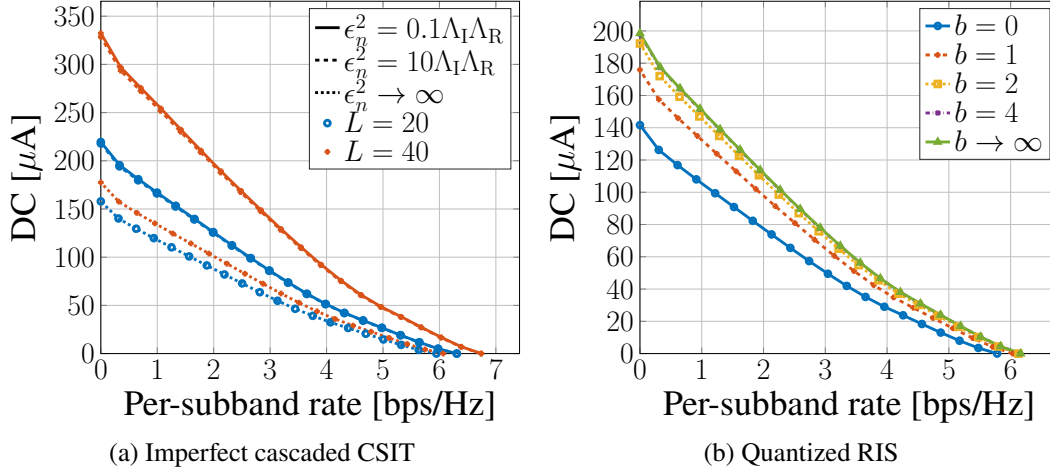


Fig. 1.13 Average R-E region with imperfect cascaded CSIT and quantized RIS for $M = 1$, $N = 16$, $L = 20$, $\sigma_n^2 = -40$ dBm, $B = 10$ MHz and $d_H = d_V = 2$ m. $\epsilon_n = 0$ and $\epsilon_n = \infty$ correspond respectively to perfect CSIT and no CSIT (and random RIS); $b = 0$ and $b \rightarrow \infty$ correspond respectively to no RIS and continuous RIS.

reduce the circuit complexity and control overhead.⁸ Figure 1.13(b) suggests that even $b = 1$ (i.e., two-state reflection) brings considerable R-E gain over the benchmark scheme without RIS, and the performance gap between $b = 4$ and unquantized RIS is negligible. These observations demonstrate the advantage of the proposed joint waveform, active and passive beamforming design in practical RIS-aided SWIPT systems.

1.5 Conclusion and Future Works

This paper investigated the R-E tradeoff of a single user employing practical receiving strategies in a RIS-aided multi-carrier MISO SWIPT system. Uniquely, we considered the joint waveform, active and passive beamforming design under rectifier nonlinearity to maximize the achievable R-E region. A three-stage BCD algorithm was proposed to solve the problem. In the first stage, the RIS phase shift was obtained by the SCA technique and eigen decomposition. In the second and third stages, the active precoder was derived in closed form, and the waveform amplitude and splitting ratio were optimized by the GP method. We also proposed and combined closed-form adaptive waveform schemes with a modified passive beamforming strategy to formulate a low-complexity BCD algorithm that achieves a good balance between performance and complexity. Numerical results revealed

⁸This relax-then-quantize approach can bring notable performance loss compared with direct optimization over the discrete phase shift set, especially for a small b (i.e., low-resolution RIS) [48].

significant R-E gains by modeling harvester nonlinearity in the RIS-aided SWIPT design. Unlike active antennas, RIS elements cannot be designed independently across frequencies, but can integrate coherent combining and equal gain transmission to enable constructive reflection and flexible subchannel design. Compared to the conventional no-RIS system, the RIS mainly affects the effective channel instead of the waveform design.

One particular unanswered question of this paper is how to design waveform, active and passive beamforming in a multi-user multi-carrier RIS-aided SWIPT system. Also, harvester saturation effect and practical RIS models with amplitude-phase coupling [24], angle-dependent reflection [47], frequency-dependent reflection, and/or partially/fully-connected architecture [49] could be considered in future works.

References

- [1] B. Clerckx, R. Zhang, R. Schober, D. W. K. Ng, D. I. Kim, and H. V. Poor, “Fundamentals of wireless information and power transfer: From RF energy harvester models to signal and system designs,” *IEEE Journal on Selected Areas in Communications*, vol. 37, no. 1, pp. 4–33, Jan. 2019.
- [2] L. R. Varshney, “Transporting information and energy simultaneously,” in *2008 IEEE International Symposium on Information Theory*. IEEE, Jul. 2008, pp. 1612–1616.
- [3] X. Zhou, R. Zhang, and C. K. Ho, “Wireless information and power transfer: Architecture design and rate-energy tradeoff,” *IEEE Transactions on Communications*, vol. 61, no. 11, pp. 4754–4767, Nov. 2013.
- [4] R. Zhang and C. K. Ho, “MIMO broadcasting for simultaneous wireless information and power transfer,” *IEEE Transactions on Wireless Communications*, vol. 12, no. 5, pp. 1989–2001, May 2013.
- [5] J. Park and B. Clerckx, “Joint wireless information and energy transfer in a k-user MIMO interference channel,” *IEEE Transactions on Wireless Communications*, vol. 13, no. 10, pp. 5781–5796, Oct. 2014.
- [6] M. Trotter, J. Griffin, and G. Durgin, “Power-optimized waveforms for improving the range and reliability of RFID systems,” in *2009 IEEE International Conference on RFID*. IEEE, Apr. 2009, pp. 80–87.
- [7] B. Clerckx and J. Kim, “On the beneficial roles of fading and transmit diversity in wireless power transfer with nonlinear energy harvesting,” *IEEE Transactions on Wireless Communications*, vol. 17, no. 11, pp. 7731–7743, Nov. 2018.
- [8] B. Clerckx and E. Bayguzina, “Waveform design for wireless power transfer,” *IEEE Transactions on Signal Processing*, vol. 64, no. 23, pp. 6313–6328, Dec. 2016.
- [9] J. Kim, B. Clerckx, and P. D. Mitcheson, “Experimental analysis of harvested energy and throughput trade-off in a realistic SWIPT system,” in *2019 IEEE Wireless Power Transfer Conference (WPTC)*. IEEE, Jun. 2019, pp. 1–5.
- [10] ———, “Signal and system design for wireless power transfer: Prototype, experiment and validation,” *IEEE Transactions on Wireless Communications*, vol. 19, no. 11, pp. 7453–7469, Nov. 2020.
- [11] J. Kim and B. Clerckx, “Range expansion for wireless power transfer using joint beamforming and waveform architecture: An experimental study in indoor environment,” *IEEE Wireless Communications Letters*, vol. 10, no. 6, pp. 1237–1241, Jun. 2021.

- [12] B. Clerckx and E. Bayguzina, "Low-complexity adaptive multisine waveform design for wireless power transfer," *IEEE Antennas and Wireless Propagation Letters*, vol. 16, no. 1, pp. 2207–2210, 2017.
- [13] J. Kim, B. Clerckx, and P. D. Mitcheson, "Prototyping and experimentation of a closed-loop wireless power transmission with channel acquisition and waveform optimization," in *2017 IEEE Wireless Power Transfer Conference (WPTC)*. IEEE, May 2017, pp. 1–4.
- [14] B. Clerckx, "Wireless information and power transfer: Nonlinearity, waveform design, and rate-energy tradeoff," *IEEE Transactions on Signal Processing*, vol. 66, no. 4, pp. 847–862, Feb. 2018.
- [15] M. Varasteh, B. Rassouli, and B. Clerckx, "On capacity-achieving distributions for complex AWGN channels under nonlinear power constraints and their applications to SWIPT," *IEEE Transactions on Information Theory*, vol. 66, no. 10, pp. 6488–6508, Oct. 2020.
- [16] —, "SWIPT signaling over frequency-selective channels with a nonlinear energy harvester: Non-zero mean and asymmetric inputs," *IEEE Transactions on Communications*, vol. 67, no. 10, pp. 7195–7210, Oct. 2019.
- [17] M. Varasteh, J. Hoydis, and B. Clerckx, "Learning to communicate and energize: Modulation, coding, and multiple access designs for wireless information-power transmission," *IEEE Transactions on Communications*, vol. 68, no. 11, pp. 6822–6839, Nov. 2020.
- [18] R. Anwar, L. Mao, and H. Ning, "Frequency selective surfaces: A review," *Applied Sciences*, vol. 8, no. 9, p. 1689, Sep. 2018.
- [19] T. J. Cui, M. Q. Qi, X. Wan, J. Zhao, and Q. Cheng, "Coding metamaterials, digital metamaterials and programmable metamaterials," *Light: Science & Applications*, vol. 3, no. 10, pp. e218–e218, Oct. 2014.
- [20] C. Liaskos, S. Nie, A. Tsioliariidou, A. Pitsillides, S. Ioannidis, and I. Akyildiz, "Realizing wireless communication through software-defined hypersurface environments," in *2018 IEEE 19th International Symposium on "A World of Wireless, Mobile and Multimedia Networks" (WoWMoM)*. IEEE, Jun. 2018, pp. 14–15.
- [21] Q. Wu and R. Zhang, "Intelligent reflecting surface enhanced wireless network: Joint active and passive beamforming design," in *2018 IEEE Global Communications Conference (GLOBECOM)*, vol. 18, no. 11. IEEE, Dec. 2018, pp. 1–6.
- [22] —, "Beamforming optimization for intelligent reflecting surface with discrete phase shifts," in *ICASSP 2019 - 2019 IEEE International Conference on Acoustics, Speech and Signal Processing (ICASSP)*. IEEE, May 2019, pp. 7830–7833.
- [23] —, "Intelligent reflecting surface enhanced wireless network via joint active and passive beamforming," *IEEE Transactions on Wireless Communications*, vol. 18, no. 11, pp. 5394–5409, Nov. 2019.

- [24] S. Abeywickrama, R. Zhang, and C. Yuen, "Intelligent reflecting surface: Practical phase shift model and beamforming optimization," in *ICC 2020 - 2020 IEEE International Conference on Communications (ICC)*. IEEE, Jun. 2020, pp. 1–6.
- [25] Q.-U.-A. Nadeem, A. Kammoun, A. Chaaban, M. Debbah, and M.-S. Alouini, "Intelligent reflecting surface assisted wireless communication: Modeling and channel estimation," *arXiv:1906.02360*, pp. 1–7, Jun. 2019.
- [26] C. You, B. Zheng, and R. Zhang, "Intelligent reflecting surface with discrete phase shifts: Channel estimation and passive beamforming," in *ICC 2020 - 2020 IEEE International Conference on Communications (ICC)*. IEEE, Jun. 2020, pp. 1–6.
- [27] J.-M. Kang, "Intelligent reflecting surface: Joint optimal training sequence and reflection pattern," *IEEE Communications Letters*, vol. 24, no. 8, pp. 1784–1788, Aug. 2020.
- [28] P. Wang, J. Fang, H. Duan, and H. Li, "Compressed channel estimation for intelligent reflecting surface-assisted millimeter wave systems," *IEEE Signal Processing Letters*, vol. 27, pp. 905–909, 2020.
- [29] Q. Wu and R. Zhang, "Towards smart and reconfigurable environment: Intelligent reflecting surface aided wireless network," *IEEE Communications Magazine*, vol. 58, no. 1, pp. 106–112, Jan. 2020.
- [30] L. Dai, B. Wang, M. Wang, X. Yang, J. Tan, S. Bi, S. Xu, F. Yang, Z. Chen, M. D. Renzo, C.-B. Chae, and L. Hanzo, "Reconfigurable intelligent surface-based wireless communications: Antenna design, prototyping, and experimental results," *IEEE Access*, vol. 8, pp. 45 913–45 923, 2020.
- [31] Q. Wu and R. Zhang, "Weighted sum power maximization for intelligent reflecting surface aided SWIPT," *IEEE Wireless Communications Letters*, vol. 9, no. 5, pp. 586–590, May 2020.
- [32] Y. Tang, G. Ma, H. Xie, J. Xu, and X. Han, "Joint transmit and reflective beamforming design for IRS-assisted multiuser MISO SWIPT systems," in *ICC 2020 - 2020 IEEE International Conference on Communications (ICC)*. IEEE, Jun. 2020, pp. 1–6.
- [33] Q. Wu and R. Zhang, "Joint active and passive beamforming optimization for intelligent reflecting surface assisted SWIPT under QoS constraints," *IEEE Journal on Selected Areas in Communications*, vol. 38, no. 8, pp. 1735–1748, Aug. 2020.
- [34] D. Xu, X. Yu, V. Jamali, D. W. K. Ng, and R. Schober, "Resource allocation for large IRS-assisted SWIPT systems with non-linear energy harvesting model," in *2021 IEEE Wireless Communications and Networking Conference (WCNC)*. IEEE, Mar. 2021, pp. 1–7.
- [35] R. Hansen, "Relationships between antennas as scatterers and as radiators," *Proceedings of the IEEE*, vol. 77, no. 5, pp. 659–662, May 1989.
- [36] G. H. Golub and C. F. Van Loan, *Matrix Computations*. Baltimore, MD, USA: Johns Hopkins University Press, 2013.

- [37] T. Adali and S. Haykin, Eds., *Adaptive Signal Processing: Next Generation Solutions*. Hoboken, NJ, USA: Wiley, Mar. 2010.
- [38] Z.-q. Luo, W.-k. Ma, A. So, Y. Ye, and S. Zhang, “Semidefinite relaxation of quadratic optimization problems,” *IEEE Signal Processing Magazine*, vol. 27, no. 3, pp. 20–34, May 2010.
- [39] M. Grant, S. Boyd, and Y. Ye, “CVX: MATLAB software for disciplined convex programming,” 2016. [Online]. Available: <http://cvxr.com/cvx>
- [40] S. Boyd, S.-J. Kim, L. Vandenberghe, and A. Hassibi, “A tutorial on geometric programming,” *Optimization and Engineering*, vol. 8, no. 1, pp. 67–127, May 2007.
- [41] M. Chiang, *Geometric Programming for Communication Systems*. Boston, MA: Now, 2005.
- [42] D. Tse and P. Viswanath, *Fundamentals of Wireless Communication*. Cambridge University Press, May 2005.
- [43] L. Grippo and M. Sciandrone, “On the convergence of the block nonlinear gauss–seidel method under convex constraints,” *Operations Research Letters*, vol. 26, no. 3, pp. 127–136, Apr. 2000.
- [44] V. Erceg, L. Schumacher, P. Kyritsi, A. Molisch, D. S. Baum, A. Y. Gorokhov, C. Oestges, Q. Li, K. Yu, N. Tal, B. Dijkstra, A. Jagannatham, C. Lanzl, V. J. Rhodes, J. Medbo, D. Michelson, M. Webster, E. Jacobsen, D. Cheung, C. Prettie, M. Ho, S. Howard, B. Bjerke, L. Jengx, H. Sampath, S. Catreux, S. Valle, A. Poloni, A. Forenza, and R. W. Heath, “IEEE P802.11 wireless LANs TGn channel models,” *IEEE 802.11-03/940r4*, 2004.
- [45] S. Li, K. Yang, M. Zhou, J. Wu, L. Song, Y. Li, and H. Li, “Full-duplex amplify-and-forward relaying: Power and location optimization,” *IEEE Transactions on Vehicular Technology*, vol. 66, no. 9, pp. 8458–8468, Sep. 2017.
- [46] O. Ozdogan, E. Bjornson, and E. G. Larsson, “Intelligent reflecting surfaces: Physics, propagation, and pathloss modeling,” *IEEE Wireless Communications Letters*, vol. 9, no. 5, pp. 581–585, May 2020.
- [47] W. Tang, M. Z. Chen, X. Chen, J. Y. Dai, Y. Han, M. Di Renzo, Y. Zeng, S. Jin, Q. Cheng, and T. J. Cui, “Wireless communications with reconfigurable intelligent surface: Path loss modeling and experimental measurement,” *IEEE Transactions on Wireless Communications*, vol. 20, no. 1, pp. 421–439, Jan. 2021.
- [48] Q. Wu and R. Zhang, “Beamforming optimization for wireless network aided by intelligent reflecting surface with discrete phase shifts,” *IEEE Transactions on Communications*, vol. 68, no. 3, pp. 1838–1851, Mar. 2020.
- [49] S. Shen, B. Clerckx, and R. Murch, “Modeling and architecture design of reconfigurable intelligent surfaces using scattering parameter network analysis,” *IEEE Transactions on Wireless Communications*, pp. 1–1, Nov. 2021.